1993

# Computation of the integrated aerodynamic and propulsive flowfields of a generic hypersonic space plane

Ganesh Wadawadigi
*Iowa State University*

Order Number 9414032

# Computation of the integrated aerodynamic and propulsive flowfields of a generic hypersonic space plane

Wadawadigi, Ganesh, Ph.D.

Iowa State University, 1993

U·M·I
300 N. Zeeb Rd.
Ann Arbor, MI 48106

**Computation of the integrated aerodynamic and propulsive flowfields of a generic hypersonic space plane**

by

Ganesh Wadawadigi

A Dissertation Submitted to the

Graduate Faculty in Partial Fulfillment of the

Requirements for the Degree of

DOCTOR OF PHILOSOPHY

Department: Aerospace Engineering and Engineering Mechanics
Major: Aerospace Engineering

Approved:

Signature was redacted for privacy.

In Charge of Major Work

Signature was redacted for privacy.

For the Major Department

Signature was redacted for privacy.

For the Graduate College

Members of the Committee:

Signature was redacted for privacy.

Iowa State University
Ames, Iowa

1993

## TABLE OF CONTENTS

## LIST OF FIGURES

## LIST OF TABLES

## ACKNOWLEDGEMENTS

I wish to express my sincere appreciation and gratitude to Prof. John C. Tannehill for his guidance and support during my graduate studies and research. I am thankful to Drs. Scott L. Lawrence, Thomas A. Edwards, Gregory A. Molvik and Johnny R. Narayan of NASA Ames Research Center for sharing their technical expertise. I would also like to acknowledge the FAST (Flow Analysis Software Toolkit) development team at the Numerical Aerodynamics Simulation (NAS) division of NASA Ames Research Center for their prompt and helpful user support and for developing excellent flow visualization software. Most of all, I am deeply indebted to my parents for their numerous sacrifices and moral encouragement throughout my education.

All the computations were performed on the CCF CRAY–YMP and CRAY–C90 at NASA Ames Research Center. This work was supported by NASA Ames Research Center under Grants NAG 2–502 and NAG 2–776. Dr. Thomas A. Edwards was the Technical Monitor for these grants.

# CHAPTER 1. INTRODUCTION

A typical hypersonic space place is envisioned to be an air–breathing vehicle equipped with a supersonic combustion ramjet (scramjet) engine. One of the most important design aspects of a hypersonic space plane is the propulsion/airframe integration. The advantages of such a design in providing increased efficiencies has been well established [1,2]. The shape of the forebody and aftbody play a prominent role. The forebody acts as a compression region providing a highly compressed flow to the scramjet inlet, while the aftbody serves as a part of the nozzle, providing significant thrust to the space plane.

The operating conditions of a flight vehicle dictate the choice of the fuel. The fuel of interest may be characterized by the properties [3] shown in Fig. 1.1. With increasing cruise Mach numbers, the fuel of choice typically changes from the conventional kerosene fuels for lower speeds to cryogenic fuels like methane ($CH_4$) or liquid hydrogen ($H_2$) for hypersonic speeds. Hydrogen is the candidate fuel of choice for hypersonic space planes. The reaction kinetics of $H_2$-air are particularly rapid, thus minimizing the combustion length and residence time in the supersonic combustor. Due to the low density and low temperature requirements, the stowability is one of the major limitations of liquid hydrogen. But this is more than made up by its refigerative capacity, which is the greatest of any known fuel. In addition, hydrogen may be used to cool both the internal (engine) and external flow surfaces.

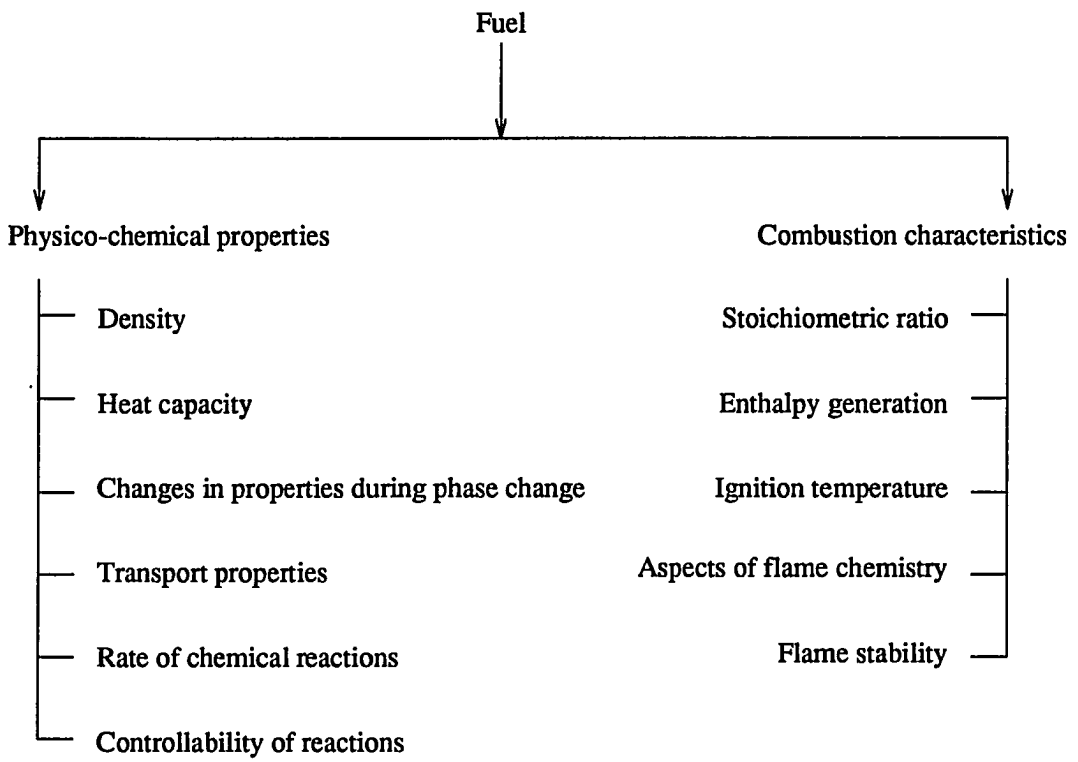


Figure 1.1: Properties of fuel

The high temperature and high Mach number flight conditions of hypersonic space planes result in strong shocks embedded in the external flowfield. These severe conditions also lead to chemical reactions in the air surrounding the vehicle. This, coupled with the complicated combustion processes occurring in the scramjet, make ground testing of such configurations extremely difficult and expensive. In addition, the non–scalability of the scramjet combustion flowfields, due to the limited size of the ground testing facilities, reduce the effectiveness of experimental tests. Thus, computational fluid dynamics (CFD) plays an important role in the analysis of the external as well as the internal flowfields of such

configurations. Both the fluid mechanics and chemical physics can be modeled numerically. Depending on the complexity of the numerical model, simulations can then be performed to various degrees of intricacies to study the flow structure and the physical/chemical processes occurring in the flowfield. A computationally efficient method is obviously important in order to proceed through the design and analysis process.

## Previous Research

The numerical simulation of both external and internal hypersonic flows with finite–rate chemistry has evolved rapidly in the last few years. Numerous numerical methods have been proposed that either solve the unsteady Navier–Stokes (NS) equations [4-14] or the steady parabolized Navier–Stokes (PNS) equations [11,15-30]. Typically the NS solvers require one to two orders-of-magnitude more computational time and storage as compared to the PNS solvers. The unsteady NS solvers are required if the inviscid portion of the flow becomes subsonic, such as in the nose region of a blunt vehicle. Aft of the nose region, the flow can be efficiently solved using a PNS code if the inviscid portion of the flow remains supersonic and if there is no streamwise flow separation.

Lawrence *et al.* [31,32] have developed a robust upwind (perfect gas) PNS code (UPS code) which solves the PNS equations using a finite–volume, upwind TVD (Total Variation Diminishing) method based on Roe's approximate Riemann solver [33]. The dissipation term associated with this scheme is sufficiently adaptive to various flow conditions so that no user-specified smoothing is required. This eliminates the problem of determining the correct amount of smoothing which "plagued" many of the previous centrally-differenced PNS codes. The two–dimensional (2–D) [31] and three–dimensional (3–D) [32] versions of the UPS code have been extended to permit both equilibrium [22,28] and nonequilibrium [23,30] (finite–rate, chemically reacting) airflow computations. For nonequilibrium

flows, the fluid dynamic and species continuity equations are solved in a loosely–coupled manner. The coupling can be enhanced with an iterative procedure if necessary. The advantages of using a loosely-coupled approach are two–fold:

1. A more complex chemistry model can be added without modifying the solution procedure of the fluids.

2. The system of equations for the chemistry can be solved without the need for computationally expensive block inversions.

The UPS code has been rigorously validated by comparing results with other codes and experimental results for a wide range of flow conditions [28,30,32,34-36].

## Current Work

Turbulence plays a key role in the complex scramjet flowfield. Hence, the modeling of turbulent mixing and combustion processes involved in the internal (scramjet) flowfield are important for the design and performance of the engine. In the present work, the 3–D UPS code has been enhanced to permit the calculation of internal flows with hydrogen–air chemistry [37]. This chemistry model consists of eleven reactions and nine species [38]. Two kinds of turbulence models have been incorporated:

1. Algebraic turbulence model: The modified version of the algebraic turbulence model of Baldwin–Lomax [39] proposed by Hung *et al.* [40] is used. This model is based on a 'modified distance', suitable for three dimensional corner flows. This model was chosen for its inherent simplicity and suitability for complex flows with length scales that are not well defined.

2. Two–equation turbulence model: The $k - \epsilon$ turbulence model of Jones and Launder [41] is used. The turbulence transport equations are solved uncoupled from the fluids. A finite–volume formulation is used with an upwind–biased TVD scheme, similar to the fluid dynamics equations. Options for choosing either the high Reynolds number form or the low Reynolds number form of the equations, as well as a choice of either a first, second, or third order accurate numerical scheme have been provided. Two kinds of compressibility corrections have been incorporated:

   - Zeman compressibility correction [42].
   - Sarkar and Balakrishnan compressibility correction [43].

With the algebraic turbulence model employed, the code is applied to two internal flow test cases [37]. These test cases model portions of the flowfield in a typical scramjet engine of a hypersonic vehicle. The first case consists of the Burrows–Kurkov supersonic combustion experiment [44] in which hydrogen was injected tangentially at sonic speed through a slot in the floor of a test section with a supersonic ($M_\infty = 2.44$) vitiated airstream. The location of the ignition and the species profiles and total temperature profiles at the exit plane are compared with the experiment. In the second test case, the code is used to compute the shock induced combustion of a premixed, supersonic ($M_\infty = 7.0$) airstream entering a 3–D duct with a 15-deg compression ramp.

With the addition of the two–equation turbulence model, the code can now provide more accurate simulations of the complex flowfields around hypersonic vehicles. Four test cases are computed to validate [45] the two–equation turbulence model option. All aspects of the turbulence model are tested including the high and low Reynolds number form of the turbulence transport equations, and hydrogen–air combustion due to turbulence enhanced

mixing. These test cases are also indicative of the flows encountered in the scramjet engine of a hypersonic vehicle. The first test case is the 2–D supersonic free–shear layer calculation of Viegas *et al.* [46]. This involves two parallel supersonic streams of perfect gas initially separated by a splitter plate with no boundary layer thickness. The computed results are compared with the Navier–Stokes calculation of Viegas *et al.* The second test case is a supersonic, perfect gas, 2–D flat plate boundary layer. The validation is performed using the results from Van Driest II theory [47]. Comparisons are also made with the Baldwin–Lomax turbulence model. The third test case consists of the Burrows–Kurkov supersonic combustion experiment. The fourth test case was devised as a consequence of the paucity of fully documented experimental data for supersonic, hydrogen–air combustion cases for validation of CFD codes. This numerical experiment consists of a supersonic, combusting, free-shear layer [48]. The setup is similar to the test case of Viegas *et al.*, but the two streams are of different chemical composition. The lower stream contains nitrogen and oxygen, whereas the upper stream contains nitrogen and hydrogen. The computed profiles of the species mass fraction and flow variables are compared with the results from the STUFF code [11]. The STUFF code is a PNS code which solves both the chemistry and turbulence equations in a strongly–coupled form using a temporal Riemann solver.

Finally, the capability of the new code in being able to efficiently solve the three dimensional, integrated aerodynamic and propulsive flowfields of a generic hypersonic space plane is demonstrated [49]. The configuration chosen is the Test Technology Demonstrator (TTD). Two test cases are considered to study the flow structure around such a configuration. The first one is a power-off condition, where the fluid medium is assumed to be air in chemical nonequilibrium. The second scenario is that of a power-on condition with a stoichiometric mixture of $H_2$–air injected at the throat of the scramjet to simulate the com-

bustion conditions. The cruise conditions chosen are at an altitude of 100,000 feet (30.5 km) and a freestream Mach number of 10.05, which results in a shock-on-lip condition. Both cases include a tip–to–tail calculation and assume a sharp–nosed configuration.

# CHAPTER 2. GOVERNING EQUATIONS

## Parabolized Navier–Stokes Equations

The PNS equations are used in the present study to model the fluid dynamics. These equations are obtained from the steady, compressible Navier–Stokes equations by neglecting streamwise viscous terms and by retaining only a fraction of the streamwise pressure gradient term in the subsonic layer in order to eliminate ellipticity in the marching direction. The latter is accomplished using Vigneron's technique [50] in conjunction with the extension to chemically–reacting flows by Prabhu *et al.* [18]. The PNS equations expressed in generalized coordinates $(\xi, \eta, \zeta)$, are given by

$$\mathbf{E}_\xi + \mathbf{F}_\eta + \mathbf{G}_\zeta = 0 \tag{2.1}$$

where

$$\begin{aligned}
\mathbf{E}_\xi &= \left(\frac{\xi_x}{J}\right)\mathbf{E}_i + \left(\frac{\xi_y}{J}\right)\mathbf{F}_i + \left(\frac{\xi_z}{J}\right)\mathbf{G}_i \\
\mathbf{F}_\eta &= \left(\frac{\eta_x}{J}\right)(\mathbf{E}_i - \mathbf{E}_v^*) + \left(\frac{\eta_y}{J}\right)(\mathbf{F}_i - \mathbf{F}_v^*) + \left(\frac{\eta_z}{J}\right)(\mathbf{G}_i - \mathbf{G}_v^*) \\
\mathbf{G}_\zeta &= \left(\frac{\zeta_x}{J}\right)(\mathbf{E}_i - \mathbf{E}_v^*) + \left(\frac{\zeta_y}{J}\right)(\mathbf{F}_i - \mathbf{F}_v^*) + \left(\frac{\zeta_z}{J}\right)(\mathbf{G}_i - \mathbf{G}_v^*)
\end{aligned} \tag{2.2}$$

The inviscid and viscous flux vectors are given by

$$\mathbf{E}_i = \left\{\rho u, \rho u^2 + p, \rho uv, \rho uw, (E_t + p)\,u\right\}^T$$

$$
\begin{aligned}
\mathbf{F}_i &= \left\{\rho v, \rho uv, \rho v^2 + p, \rho vw, (E_t + p)\, v\right\}^T \\
\mathbf{G}_i &= \left\{\rho w, \rho uw, \rho vw, \rho w^2 + p, (E_t + p)\, w\right\}^T \\
\mathbf{E}_v &= \{0, \tau_{xx}, \tau_{xy}, \tau_{xz}, u\tau_{xx} + v\tau_{xy} + w\tau_{xz} - q_x\}^T \\
\mathbf{F}_v &= \{0, \tau_{yx}, \tau_{yy}, \tau_{yz}, u\tau_{yx} + v\tau_{yy} + w\tau_{yz} - q_y\}^T \\
\mathbf{G}_v &= \{0, \tau_{zx}, \tau_{zy}, \tau_{zz}, u\tau_{zx} + v\tau_{zy} + w\tau_{zz} - q_z\}^T
\end{aligned}
\tag{2.3}
$$

where $E_t = \rho\{e + \frac{1}{2}(u^2 + v^2 + w^2)\}$

The effect of mass diffusion of the species is accounted for by adding the following component to the heat flux terms $(q_x, q_y, q_z)$

$$
\rho \sum_{s=1}^{n} c_s \mathbf{U}_s h_s \tag{2.4}
$$

where $\mathbf{U}_s$ is the diffusion velocity of species $s$, $c_s$ is the species mass fraction, and $h_s$ is the species enthalpy. The superscript asterisks on the viscous flux vectors in Eq. 2.2 indicate that the derivatives with respect to $\xi$ have been dropped. In the above equations, $p$ is the pressure; $\rho$ is the density; $u, v$, and $w$ are the velocity components in the $x, y$, and $z$ directions, respectively; $e$ is the internal energy; $\tau$ is the viscous stress; and $q$ is the heat flux due to conduction. The dependent variables have been non-dimensionalized as follows:

$$
x, y, z = \frac{x^*, y^*, z^*}{L^*} \qquad p = \frac{p^*}{\rho_\infty^* V_\infty^{*2}} \qquad e = \frac{e^*}{V_\infty^{*2}} \qquad u, v, w = \frac{u^*, v^*, w^*}{V_\infty^*}
$$

$$
\mu = \frac{\mu^*}{\mu_\infty^*} \qquad \rho = \frac{\rho^*}{\rho_\infty^*} \qquad \kappa = \frac{\kappa^*}{\kappa_\infty^*} \qquad T = \frac{T^*}{T_\infty^*}
$$

The species continuity equation is given by

$$
\frac{\partial \rho_s}{\partial t} + \nabla \cdot (\rho_s \mathbf{V}_s) = \omega_s \qquad s = 1, 2, \ldots, n \tag{2.5}
$$

where $\mathbf{V}_s$ is the sum of the fluid velocity $\mathbf{V}$ and the species diffusion velocity $\mathbf{U}_s$. The species density is denoted by $\rho_s$ and the term $\omega_s$ is the mass production or depletion rate

of the species $s$ which is a function of the temperature, density and the mass concentration of the reactants constituting the mixture. The subscript $s$ denotes the species index. Using the global continuity equation and assuming Fick's law for mass diffusion, the above form of the species continuity equation is simplified to

$$\rho\left(\frac{\partial c_s}{\partial t} + \mathbf{V}\cdot\nabla c_s\right) = \nabla\cdot(\beta_3\rho\mathcal{D}_{sm}\nabla c_s) + \omega_s \tag{2.6}$$

where the non–dimensional quantity $\beta_3$ is

$$\beta_3 = \frac{\rho^*_\infty \mathcal{D}^*_\infty}{\mu^*_\infty \mathrm{Re}_\infty} \tag{2.7}$$

and $\mathcal{D}_{sm}$ is the multicomponent diffusion coefficient for the species $s$. In the present work, a kinetic binary diffusion coefficient $\mathcal{D}$ is used and is assumed to be the same for all the species. The species continuity equation is simplified using the PNS approximation of dropping the unsteady term and neglecting the streamwise diffusion terms. After recasting the equation into generalized coordinates, the following final form is obtained:

$$\begin{aligned}\rho\hat{U}\frac{\partial c_s}{\partial \xi} + \rho\hat{V}\frac{\partial c_s}{\partial \eta} + \rho\hat{W}\frac{\partial c_s}{\partial \zeta} - \frac{\partial}{\partial \eta}\left(A_{\eta\eta}\frac{\partial c_s}{\partial \eta} + A_{\eta\zeta}\frac{\partial c_s}{\partial \zeta}\right)\\ -\frac{\partial}{\partial \zeta}\left(A_{\zeta\zeta}\frac{\partial c_s}{\partial \zeta} + A_{\zeta\eta}\frac{\partial c_s}{\partial \eta}\right) = \frac{\omega_s}{J} \qquad s = 1,2,\ldots,n\end{aligned} \tag{2.8}$$

where

$$\begin{aligned}\hat{U} &= \left(\frac{\xi_x}{J}\right)u + \left(\frac{\xi_y}{J}\right)v + \left(\frac{\xi_z}{J}\right)w\\ \hat{V} &= \left(\frac{\eta_x}{J}\right)u + \left(\frac{\eta_y}{J}\right)v + \left(\frac{\eta_z}{J}\right)w\\ \hat{W} &= \left(\frac{\zeta_x}{J}\right)u + \left(\frac{\zeta_y}{J}\right)v + \left(\frac{\zeta_z}{J}\right)w\end{aligned} \tag{2.9}$$

and

$$A_{\eta\eta} = \beta_3\rho\mathcal{D}\left(\frac{\eta_x^2}{J} + \frac{\eta_y^2}{J} + \frac{\eta_z^2}{J}\right)$$

$$A_{\zeta\zeta} = \beta_3 \rho \mathcal{D} \left( \frac{\zeta_x^2}{J} + \frac{\zeta_y^2}{J} + \frac{\zeta_z^2}{J} \right) \tag{2.10}$$

$$A_{\eta\zeta} = A_{\zeta\eta} = \beta_3 \rho \mathcal{D} \left( \frac{\eta_x \zeta_x}{J} + \frac{\eta_y \zeta_y}{J} + \frac{\eta_z \zeta_z}{J} \right)$$

In addition to the above equations, the equation of state is used:

$$p = \frac{\beta_1 \rho T}{\mathcal{M}} \tag{2.11}$$

where the nondimensional quantity $\beta_1$ and molecular weight of the mixture $\mathcal{M}$ are given by

$$\beta_1 = \frac{\mathcal{R}_U^* T_\infty^*}{\mathcal{M}_\infty^* V_\infty^{*2}}, \qquad \mathcal{M} = \left( \sum_{s=1}^{n} \frac{c_s}{\mathcal{M}_s} \right)^{-1} \tag{2.12}$$

and $\mathcal{R}_U$ is the universal gas constant (8314.34 J/kmol/K). The ratio of specific heats, $\bar{\gamma}$ is defined as

$$\bar{\gamma} = 1 + \left( \frac{p}{\rho e^s} \right) \tag{2.13}$$

where $e^s$ is the sensible energy which can be expressed in terms of the species mass fractions ($c_s$) and the species formation enthalpy at 0°K ($h_{f_s}^0$) by

$$e^s = e - \sum_{s=1}^{n} c_s h_{f_s}^0 \tag{2.14}$$

In addition the following nondimensional quantities are used

$$\mathcal{M} = \frac{\mathcal{M}^*}{\mathcal{M}_\infty} \qquad C_{p_f} = \frac{C_{p_f}^* T_\infty^*}{V_\infty^{*2}}$$

$$\omega_s^* = \frac{\omega_s^*}{\rho_\infty^* V_\infty^*} \qquad \mathcal{D} = \frac{\mathcal{D}^*}{\mathcal{D}_\infty^*}$$

## Thermodynamic and Transport Properties

**Enthalpy and specific heat**

The enthalpies and specific heats are obtained from a table lookup procedure using the data of Ref. [51]. Cubic spline interpolation is used to the find the property at a particular temperature. Since the enthalpies in Ref. [51] are referenced to 298.15 K, they are re–referenced to 0 K in the following manner. For each species, the enthalpy at 0 K is subtracted from the enthalpy at a particular temperature T (all referenced to 298.15 K). This yields the sensible enthalpy referenced to 0 K at the temperature T. The species formation enthalpy at 0 K is then added to obtain the properly referenced enthalpy. The enthalpy and frozen specific heat of the mixture are given by

$$h^* = \sum_{s=1}^{n} c_s h_s^* \quad , \quad C_{p_f}^* = \left.\frac{dh^*}{dT^*}\right|_{c_1,\ldots,c_n} = \sum_{s=1}^{n} c_s \frac{dh_s^*}{dT^*} = \sum_{s=1}^{n} c_s C_{p,s}^* \tag{2.15}$$

where the subscripts on the differentiation denote that the mixture composition is locally frozen.

**Viscosity and thermal conductivity**

Cubic spline interpolation is employed to obtain the species viscosity ($\mu_s$) from the tabulated data given in Ref. [52]. The thermal conductivity of species $s$ is computed using Eucken's semiempirical formula:

$$\kappa_s^* = \frac{\mu_s^* \mathcal{R}^*}{\mathcal{M}_s^*} \left( C_{p,s}^* \frac{\mathcal{M}_s^*}{\mathcal{R}^*} + \frac{5}{4} \right) \tag{2.16}$$

The viscosity and thermal conductivity of the mixture are calculated using Wilke's semiempirical mixing rule [53]:

$$\mu^* = \sum_{s=1}^{n} \frac{\mathbf{X}_s \mu_s^*}{\phi_s} \quad , \quad \kappa^* = \sum_{s=1}^{n} \frac{\mathbf{X}_s \kappa_s^*}{\phi_s} \tag{2.17}$$

where

$$\mathbf{X}_s = \frac{c_s \mathcal{M}^*}{\mathcal{M}_s^*} \quad , \quad \phi_s = \sum_{r=1}^{n} \mathbf{X}_r \left(1 + \sqrt{\frac{\mu_s^*}{\mu_r^*}} \left(\frac{\mathcal{M}_r^*}{\mathcal{M}_s^*}\right)^{\frac{1}{4}}\right)^2 \left(\sqrt{8}\sqrt{1 + \frac{\mathcal{M}_r^*}{\mathcal{M}_s^*}}\right)^{-1}$$

**Diffusion coefficient**

The binary Lewis number $\mathcal{L}e$ is assumed to be the same constant for all the species and is taken to be 1.4 for air calculations and 1.0 for the combustion calculations [54,55]. The kinematic diffusion coefficient $\mathcal{D}^*$ is then computed from the definition

$$\mathcal{D}^* = \frac{\kappa^* \mathcal{L}e}{\rho^* C_{p_f}^*} \tag{2.18}$$

## Chemistry Model

The code has the option of using either perfect gas, equilibrium air, or nonequilibrium (single–temperature) chemistry models. The nonequilibrium option has two further choices:

1. Air chemistry model [56], which involves six species plus electrons ($O_2$, O, N, NO, $NO^+$, $N_2$, $e^-$) and seven reactions (Table 2.1).

2. Hydrogen–air chemistry model, which consists of nine species (H, $H_2O$, OH, O , NO, N, $H_2$, $O_2$, $N_2$) and eleven reactions (Table 2.2).

For the hydrogen–air chemistry model the reactions and the corresponding forward reaction rate variables are based on the NASP model [38] and are given in Table 2.2. The forward reaction rate for the $k$th reaction is expressed in the following expanded Arrhenius form:

$$K_{f,k}^*(T^*) = A T^{*^n} \exp(-\Theta/T^*) \tag{2.19}$$

Table 2.1: Air chemistry model

| | | | | | | | | | | |
|---|---|---|---|---|---|---|---|---|---|---|
| 1 | $O_2$ | + | $M_1$ | $\rightleftharpoons$ | 2O | + | $M_1$ | | | |
| 2 | $N_2$ | + | $M_2$ | $\rightleftharpoons$ | 2N | + | $M_2$ | | | |
| 3 | $N_2$ | + | N | $\rightleftharpoons$ | 2N | + | N | | | |
| 4 | NO | + | $M_3$ | $\rightleftharpoons$ | N | + | O | + | $M_3$ | |
| 5 | NO | + | O | $\rightleftharpoons$ | $O_2$ | + | N | | | |
| 6 | $N_2$ | + | O | $\rightleftharpoons$ | NO | + | N | | | |
| 7 | N | + | O | $\rightleftharpoons$ | $NO^+$ | + | $e^-$ | | | |

Table 2.2: $H_2$–air reactions and reaction rates

| | Reaction | | | | | | | | | | | A | n | Θ |
|---|---|---|---|---|---|---|---|---|---|---|---|---|---|---|
| 1 | H | + | $O_2$ | | | $\rightleftharpoons$ | O | + | OH | | | 1.91E+14 | 0 | 8273 |
| 2 | O | + | $H_2$ | | | $\rightleftharpoons$ | H | + | OH | | | 5.06E+04 | 2.67 | 3166 |
| 3 | OH | + | OH | | | $\rightleftharpoons$ | O | + | $H_2O$ | | | 1.50E+09 | 1.14 | 0 |
| 4 | OH | + | $H_2$ | | | $\rightleftharpoons$ | H | + | $H_2O$ | | | 2.16E+08 | 1.51 | 1726 |
| 5 | O | + | NO | | | $\rightleftharpoons$ | N | + | $O_2$ | | | 3.80E+09 | 1.0 | 20820 |
| 6 | O | + | $N_2$ | | | $\rightleftharpoons$ | NO | + | N | | | 1.82E+14 | 0 | 38370 |
| 7 | H | + | NO | | | $\rightleftharpoons$ | N | + | OH | | | 1.70E+14 | 0 | 24560 |
| 8 | H | + | H | + | M | $\rightleftharpoons$ | $H_2$ | + | M | | | 7.30E+17 | -1.0 | 0 |
| 9 | H | + | O | + | M | $\rightleftharpoons$ | OH | + | M | | | 2.60E+16 | -0.6 | 0 |
| 10 | O | + | O | + | M | $\rightleftharpoons$ | $O_2$ | + | M | | | 1.14E+17 | -1.0 | 0 |
| 11 | H | + | OH | + | M | $\rightleftharpoons$ | $H_2O$ | + | M | | | 8.62E+21 | -2.0 | 0 |

In Table 2.2 the units for the forward reaction rates are $cm^3$/mol-sec or $cm^6$/$mol^2$-sec and the third–body efficiencies are 2.5 for M = $H_2$, 16.25 for M = $H_2O$ and 1.0 for all other M.

The above chemistry models consisting of $m$ reactions, $n$ species, and $n_t$ reactants can be symbolically represented as

$$\sum_{l=1}^{n_t} \nu'_{k,l} A_l \rightleftharpoons \sum_{l=1}^{n_t} \nu''_{k,l} A_l \qquad k = 1, 2, \ldots, m \tag{2.20}$$

where $\nu'_{k,l}$ and $\nu''_{k,l}$ are the stoichiometric coefficients and $A_l$ is the chemical symbol of the $l$ th species. Using the law of mass action, the mass production/depletion rate of the species

$s$ is given by

$$\omega_s^* = \mathcal{M}_s^* \sum_{k=1}^{m} \left(\nu_{k,s}'' - \nu_{k,l}'\right) \left\{ K_{f,k}^*(T^*) \prod_{r=1}^{n_t} [\rho^* \gamma_r^*]^{\nu_{k,r}'} - K_{b,k}^*(T^*) \prod_{r=1}^{n_t} [\rho^* \gamma_r^*]^{\nu_{k,r}''} \right\} \quad (2.21)$$

The mole–mass ratios of the reactants are defined as

$$\gamma_r^* = \begin{cases} c_r/\mathcal{M}_r^* & r = 1,2,\ldots,n \\ \sum_{s=1}^{n} Z_{r,s}\gamma_s^* & r = n+1,\ldots,n_t \end{cases} \quad (2.22)$$

where $Z_{r,s}$ are the third–body efficiencies for each of the species. The backward reaction rates for the hydrogen–air calculations are obtained from

$$K_{b,k}^* = \frac{K_{f,k}^*}{K_{eq,k}^*} \qquad k = 1,2,\ldots,m \quad (2.23)$$

where $K_{eq,k}^*$ is the equilibrium constant of the $k$th reaction given by

$$K_{eq,k}^* = \left(\mathcal{R}_U' T^*\right)^{-\Delta n_k} \exp\left(\frac{-\Delta G_k^*}{\mathcal{R}_U T^*}\right) \qquad k = 1,2,\ldots,m \quad (2.24)$$

In the above equation $\mathcal{R}_U' = 82.06 \times 10^{-6}\text{m}^3\text{atm/mol/K}$ [55,57] and $\Delta n_k$ is the integer difference between the numbers of product and reactant species:

$$\Delta n_k = \sum_{s=1}^{n} \nu_{k,s}'' - \sum_{s=1}^{n} \nu_{k,s}' \qquad k = 1,2,\ldots,m \quad (2.25)$$

$$\Delta G_k^* = \sum_{s=1}^{n} \nu_{k,s}'' g_s^* - \sum_{s=1}^{n} \nu_{k,s}' g_s^* \qquad k = 1,2,\ldots,m \quad (2.26)$$

The species Gibbs free energy $g_s$ are obtained from tables in Ref. [51].

## Numerical Method

### Gasdynamic solution

A finite–volume, upwind TVD (Total Variation Diminishing) scheme is used to integrate the fluid dynamic equations. The algorithm is second–order accurate in the crossflow

plane and first–order accurate in the streamwise marching direction. The upwind algorithm is based on Roe's steady approximate Riemann solver [33] which has been modified [23] for nonequilibrium effects. Second–order central differences are used to model the mass diffusion terms and the heat flux terms. Further details of the algorithm can be found in Refs. [30,32].

**Chemistry solution**

The species continuity equations are solved in a loosely–coupled manner using a finite–volume formulation. The requirement that the mass fraction of the species sum to unity eliminates the $n$th species continuity equation:

$$c_n = 1 - \sum_{s=1}^{n-1} c_s \tag{2.27}$$

This results in requiring only $n-1$ equations to be solved. It should be noted that in all the computations performed in this study, $N_2$ was treated as an inert gas, and hence, was taken as the $n$th species. The convective terms are modeled using first–order upwind differences and the strong conservation-law form is retained by using the fluid fluxes (the coefficients of the convective terms) as known quantities from the most recent fluid integration step. The species production/depletion rate $\omega_s$ is treated as a source term and is lagged to the $n$th marching station for the present calculations.

A line Gauss–Seidel procedure with successive over–relaxation (SOR) is employed. A scalar tridiagonal solver is used to solve the resulting system of equations in an iterative manner until the residual drops below a specified tolerance level $\varepsilon$. The residual is defined as

$$| c_s^{i+1} - c_s^i | \leq \varepsilon$$

where $i+1$ is the current iteration level, and $i$ is the previous iteration level.

**Fluid/Chemistry coupling**

The coupling between the fluids and chemistry is achieved in an approximate manner. The fluid step is first taken with frozen chemistry to advance from the $n$ to the $n+1$ marching station. The fluid density and velocity computed at the new station are then used to advance the chemistry solution to the $n+1$ level. After determining the species mass fractions, mixture molecular weight, fluid density and internal energy at the $n+1$ level, the new pressure, temperature, $\bar{\gamma}$, specific enthalpy, and frozen specific heats are calculated. The coupling between the fluids and chemistry can be enhanced through the implementation of Newton iterations on the governing equations at each streamwise step [30]. This loosely coupled approach for fluids and chemistry is pictorially depicted in Fig. 2.1.

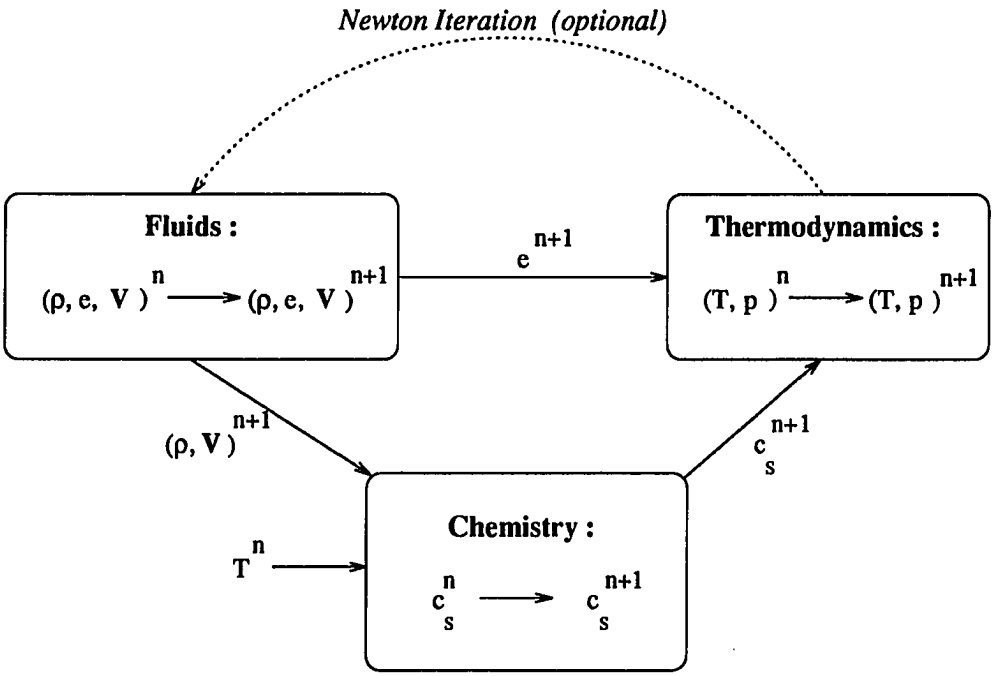


Figure 2.1: Schematic of the loosely coupled approach

The temperature is obtained using the following Newton–Raphson iterative scheme:

$$T^{*k+1} = T^{*k} - \frac{\mathcal{F}(T^{*k}) - e^*}{\mathcal{F}'(T^{*k})} \tag{2.28}$$

where

$$\mathcal{F}(T^{*k}) = \sum_{s=1}^{n} c_s \left( h_s^*(T^*) - \frac{\mathcal{R}_U T^*}{\mathcal{M}_s^*} \right) \tag{2.29}$$

$$\mathcal{F}'(T^{*k}) = \sum_{s=1}^{n} c_s \left( C_{p,s}^*(T^*) - \frac{\mathcal{R}_U}{\mathcal{M}_s^*} \right) \tag{2.30}$$

and $k$ is the iteration level. The iterations are continued until

$$| T^{*k+1} - T^{*k} | \leq \delta$$

where $\delta$ is a specified tolerance level. Once the temperature is determined, the pressure can be found from Eq. 2.11 and $\bar{\gamma}$ from Eq. 2.13.

# CHAPTER 3. ALGEBRAIC TURBULENCE MODELING

The algebraic turbulence model proposed by Baldwin–Lomax [39] and modified by Hung *et al.* [40] has been incorporated into the UPS code. This model is chosen for its inherent simplicity and its suitability for complex flows with length scales that are not well defined and is easy to implement for three–dimensional internal flows. Using the computed eddy viscosities, the turbulent thermal conductivity and mass diffusivity are calculated to account for turbulent mixing. A turbulent Prandtl number ($Pr_t$) of 0.9 is used in all the calculations presented here. Two test cases [37] are used to validate this turbulence model in the UPS code.

## Turbulence Model

The Baldwin–Lomax turbulence model is a two–layer model with the turbulent viscosity given by

$$\mu_t = \begin{cases} (\mu_t)_{inner} & \chi \leq \chi_{crossover} \\ (\mu_t)_{outer} & \chi > \chi_{crossover} \end{cases} \tag{3.1}$$

The turbulent viscosity for the inner region, $(\mu_t)_{inner}$, based on Prandtl's mixing length, is evaluated by the following expression

$$(\mu_t)_{inner} = \rho(\kappa \mathcal{D} \eta)^2 \omega \tag{3.2}$$

where $\kappa$ is the von Kármán's constant, $\mathcal{D}$ is the van Driest damping factor, and $\omega$ is the

absolute value of vorticity:

$$\begin{aligned} \kappa &= 0.4 \\ \mathcal{D} &= \left[1 - \exp\left(-y^+/A^+\right)\right]; \qquad y^+ = \frac{\chi\sqrt{\rho_w \tau_w}}{\mu_w} \quad \& \quad A^+ = 26 \\ \omega &= |\nabla \times \mathbf{V}| \end{aligned}$$

The definition of the distance $\chi$ is critical for corner flows. For the purpose of illustration, consider two perpendicular walls in a corner flow region as shown in Fig. 3.1. The walls are assumed to be aligned with the $y$ and $z$ coordinate axes as shown. Hung *et*

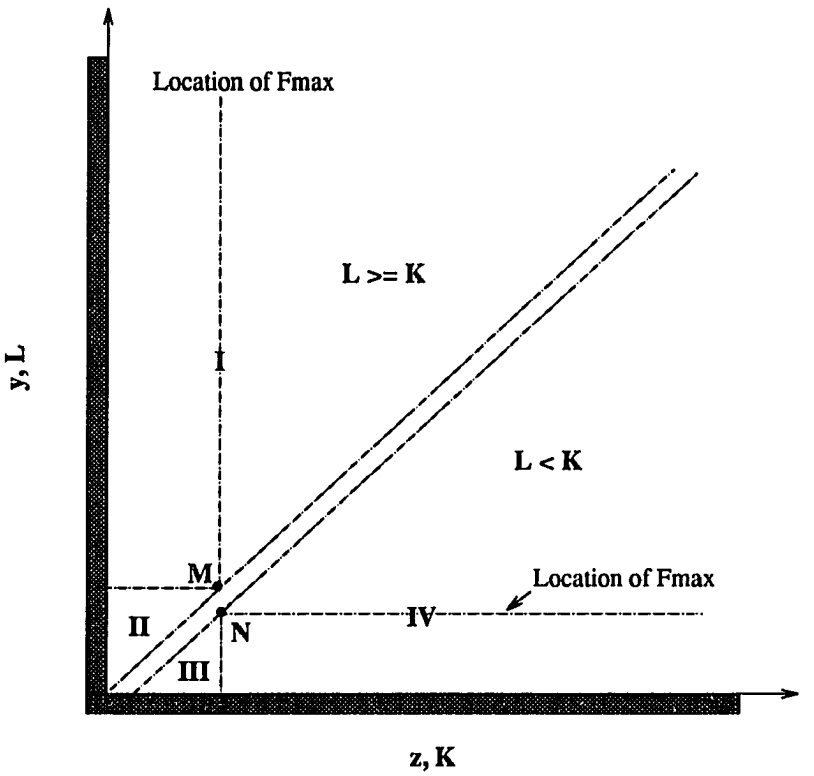


Figure 3.1: Corner flow in the KL plane

*al.* [58] defined a modified distance as shown below to account for the turbulent mixing length near a corner under the influence of both walls:

$$\chi = \frac{2yz}{y + z + \sqrt{y^2 + z^2}} \tag{3.3}$$

In the outer region, the eddy viscosity is given by

$$(\mu_t)_{outer} = (0.0168) C_{cp} \rho F_{wake} \beta \tag{3.4}$$

where

$$\begin{aligned} F(\chi) &= \chi \omega \mathcal{D} \\ F_{wake} &= \text{MIN} \begin{cases} \chi_{max} F_{max} \\ \chi_{max} C_{wk} u_e^2 / F_{max} \end{cases} \\ u_e &= \left(\sqrt{u^2 + v^2 + w^2}\right)_{\text{MAX}} - \left(\sqrt{u^2 + v^2 + w^2}\right)_{\text{MIN}} \end{aligned}$$

The quantity $F_{max}$ is the maximum value of $F$ and $\chi_{max}$ is the value of $\chi$ at which it occurs. The Klebanoff intermittency factor $\beta$ is given by

$$\beta = \left[1 + 5.5 \left(\frac{\chi C_{Kleb}}{\chi_{max}}\right)^6\right]^{-1} \tag{3.5}$$

The constants appearing in the above relations are

$$C_{cp} = 1.6, \qquad C_{wk} = 0.25, \qquad C_{Kleb} = 0.3 \tag{3.6}$$

The computational domain shown in Fig. 3.1 is subdivided into four regions (I, II, III, IV) as shown. The damping function $\mathcal{D}$ is evaluated in the various regions according to the following chart.

| Regions | $\mathcal{D}$ evaluated at wall |
|---|---|
| I & II | $z = 0$ |
| III & IV | $y = 0$ |

The search for $F_{max}$ and its corresponding $\chi_{max}$ proceeds in a direction away from the wall ($y = 0$) for region IV and from $z = 0$ for region I. The values of $F_{max}$ in the regions II and III are constants, and are equal to the values of $F_{max}$ at points M and N, respectively. For internal flows with more than one corner, the above procedure is replicated appropriately.

## Numerical Results and Discussion

Two test cases were chosen to demonstrate and validate the hydrogen–air combustion model as well as the three–dimensional internal flow capability of the code with algebraic turbulence modeling [37]. These test cases are typical of portions of the flowfield in the scramjet engine of a hypersonic vehicle. The first test case is the Burrows–Kurkov supersonic combustion experiment [44], and the second one is a three-dimensional, internal flow, shock induced combustion case.

### Test case I

In the two-dimensional Burrows–Kurkov experiment [44], combustion occurs in the supersonic shear layer produced by the sonic injection of hydrogen into a stream of vitiated air. The test section consists of two nearly parallel walls with the lower wall slightly angled down. A schematic of the experimental setup is shown in Fig. 3.2. The freestream conditions for the hydrogen jet and the vitiated air are given in Table 3.1. The wall temperature was held constant at 298 K.

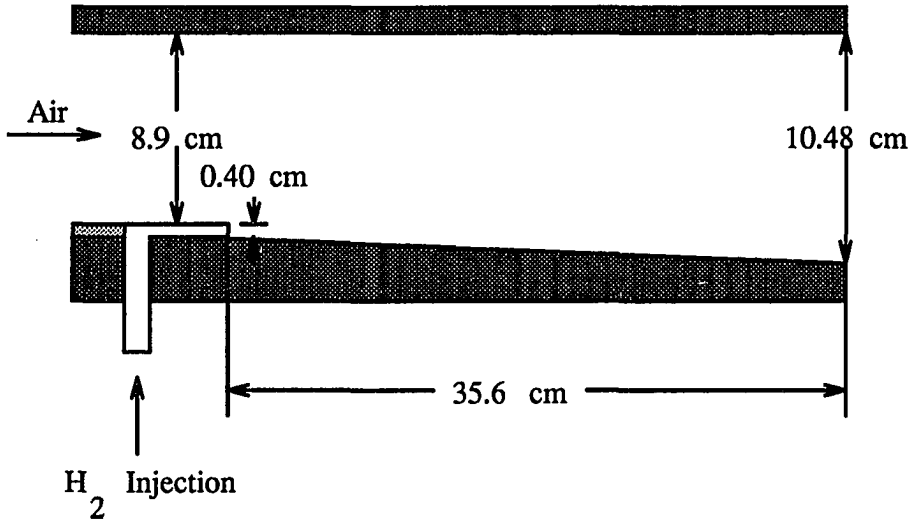


Figure 3.2: Schematic of the Burrows–Kurkov experimental setup

Table 3.1: Freestream conditions for Burrows–Kurkov experiment

| Freestream | $H_2$ jet | Vitiated airstream |
|---|---|---|
| Mach number | 1.0 | 2.44 |
| Temperature (K) | 254.0 | 1270 |
| Pressure (atm) | 1.0 | 1.0 |
| $H_2$ mass fraction | 1.0 | 0.0 |
| $H_2O$ mass fraction | 0.0 | 0.256 |
| $O_2$ mass fraction | 0.0 | 0.258 |
| $N_2$ mass fraction | 0.0 | 0.486 |

For all the calculations, a grid consisting of 101 grid points in the normal direction was used. The grid was clustered near the lower wall in order to properly resolve the shear layer. The first point off the wall was placed at $1.0\times10^{-8}$ m.

Two computations were performed with the first one being a pure mixing case. For both computations, freestream startup conditions were assumed at the x = 0 plane. For the mixing case only, the freestream temperature was set to 1150 K to match the experiment, and all of the $O_2$ in the vitiated air region was replaced by $N_2$ so that no combustion took place. The species mole fraction profiles at the exit plane (x = 35.6 cm) are compared with the experimental results in Fig. 3.3. The computed results are in excellent agreement with the experimental results.

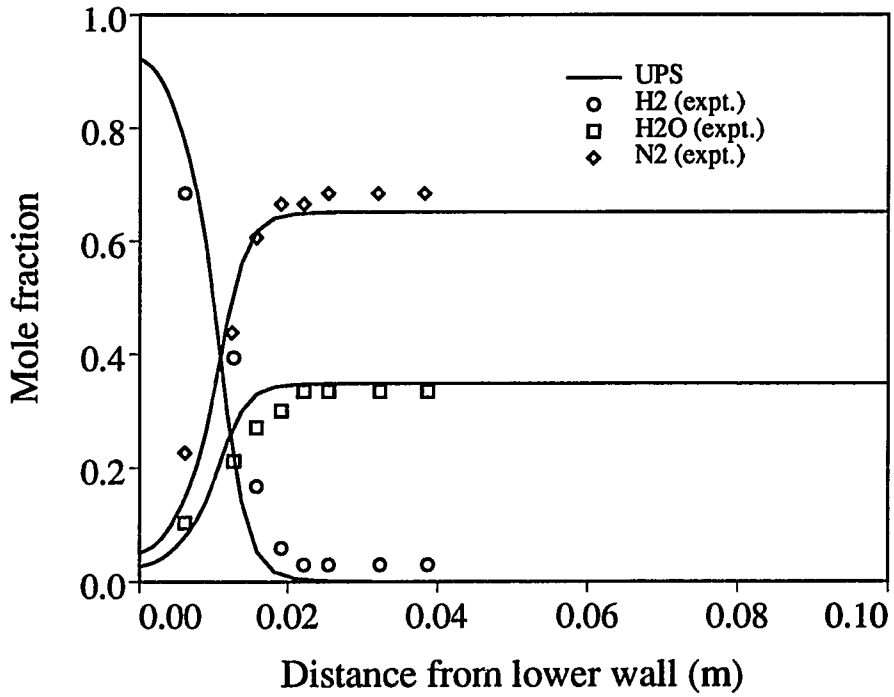


Figure 3.3: Species mole fraction profiles at the exit plane (x = 35.6 cm; pure mixing case)

The second calculation used the flow conditions listed in Table 3.1 which allow supersonic combustion to occur. Ignition, based on the mass fraction of OH species, was found to occur at about 15 cm. In the experiment, ignition occured at 25.1 cm.

The species mole fraction profiles at the exit plane are compared with the experimental results in Fig. 3.4. The flame strength denoted by the peak in the $H_2O$ profile, and the mole fraction values at the wall agree well with the experimental predictions. However, all the species profiles are shifted closer to the lower wall. Similar numerical results have been obtained by other investigators [14,25]. A series of grid refinement studies were performed to assess the effect of mesh refinement by varying the number of grid points as well as the grid stretching, and no appreciable change in the behavior of the profiles was found.

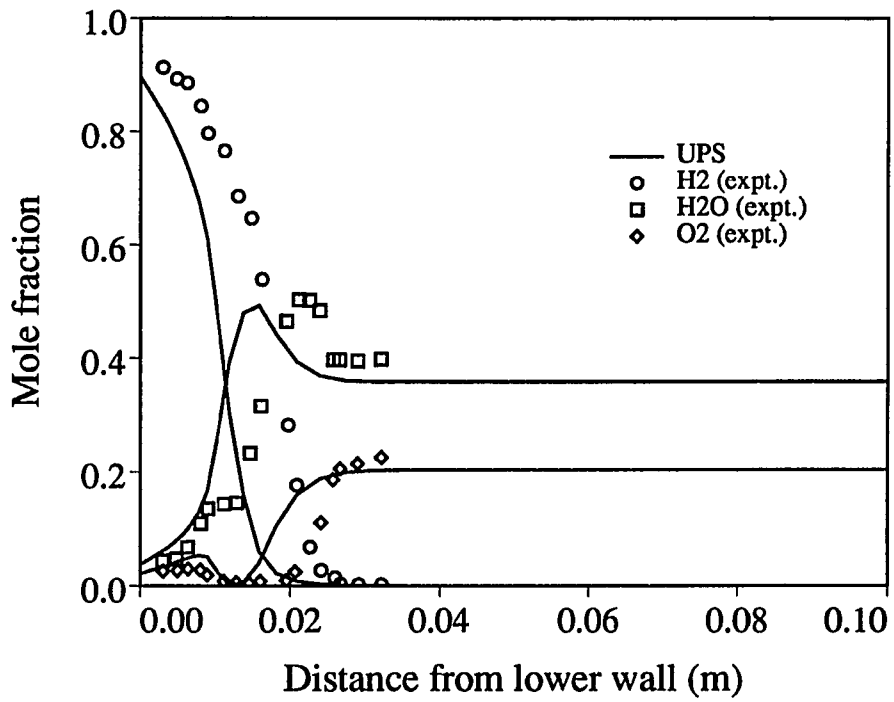


Figure 3.4: Species mole fraction profiles at the exit plane (x = 35.6 cm; combustion case)

The total temperature profiles at the exit station are compared in Fig. 3.5. The computed results, including the peak total temperature location and magnitude, compare well with the experimental data. The CPU time required for the combustion test case was $9.25 \times 10^{-4}$ s/step/grid point on the CRAY–YMP.

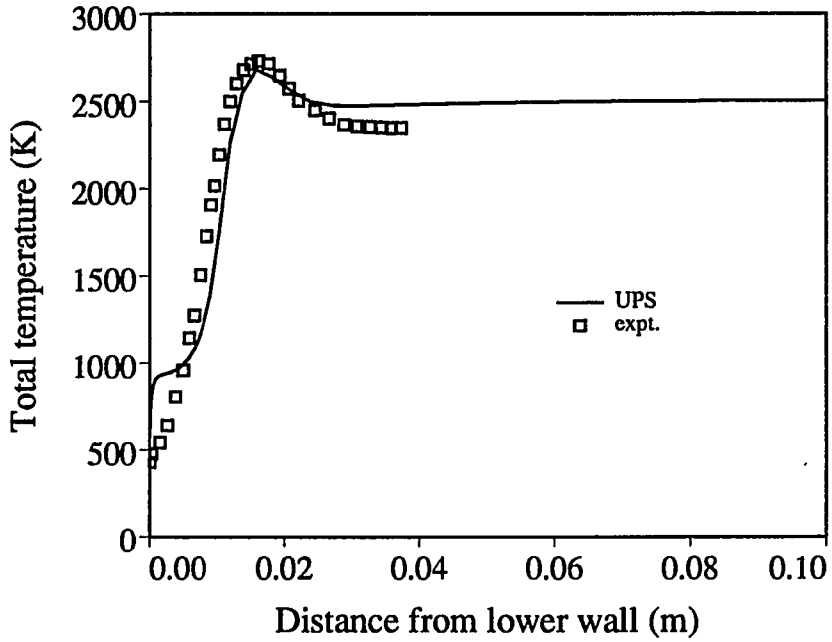


Figure 3.5: Total temperature profiles at the exit plane (x = 35.6 cm; combustion case)

**Test case II**

The second test case consists of a three–dimensional duct with a 15-deg compression ramp. Air, premixed with hydrogen, enters the duct with a freestream Mach number of 7. Combustion occurs as a result of the shock emanating from the compression ramp. The schematic of the three–dimensional duct is shown in Fig. 3.6. The side walls have been removed for the sake of clarity. The freestream flow conditions are given in Table 3.2. The flow is assumed to be turbulent and a constant wall temperature of 500 K is used.

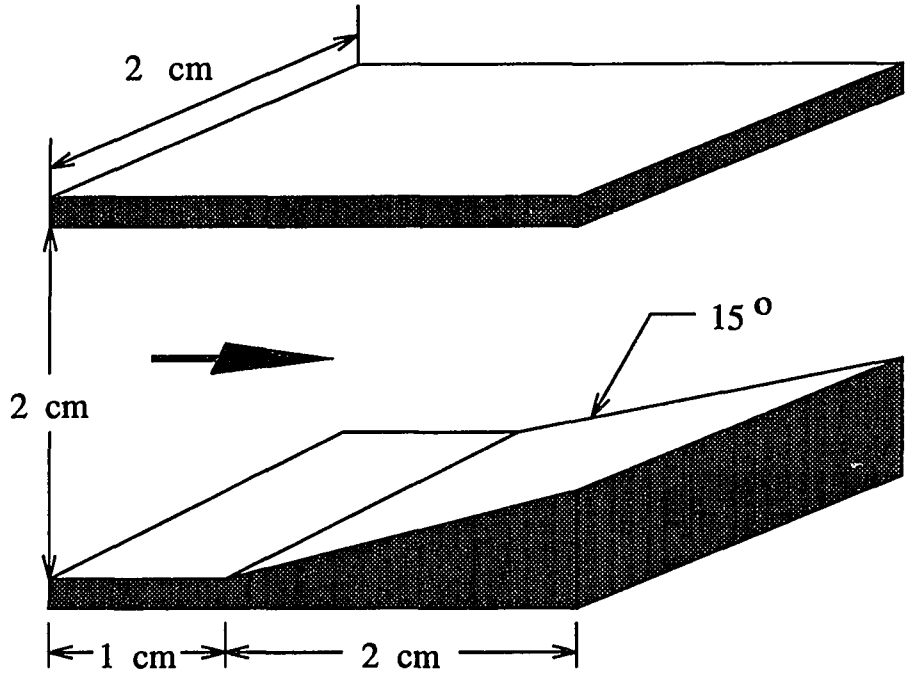


Figure 3.6: Schematic of the 3–D duct

Table 3.2: Freestream conditions for 3–D case

| | |
|---|---|
| Mach number | 7.0 |
| Reynolds number (/m) | $1.013 \times 10^6$ |
| Temperature (K) | 1200.0 |
| $H_2$ mass fraction | 0.03207 |
| $O_2$ mass fraction | 0.25447 |
| $N_2$ mass fraction | 0.71346 |

A grid consisting of 61 × 61 points at each marching station was clustered at all four walls to properly resolve the boundary layer. Due to the presence of the strong shock, smaller streamwise step sizes were taken in the vicinity of the compression corner.

The profiles of non–dimensional temperature, pressure and water vapor ($H_2O$) mole fraction, at the centerline of the exit plane (x = 3 cm) are shown in Figs. 3.7, 3.8 and 3.9, respectively. It can be seen that the compression due to the shock increases the temperature and pressure and initiates the combustion reactions which produce water vapor. The Mach contours in the streamwise symmetry plane, and in the crossflow plane at the exit of the duct are shown in Fig. 3.10. Also, shown in Fig. 3.10 are the mole fraction contours of $H_2O$ in the streamwise symmetry plane; far wall; and the crossflow plane at the exit of the duct. Once again the shock induced combustion is clearly visible.

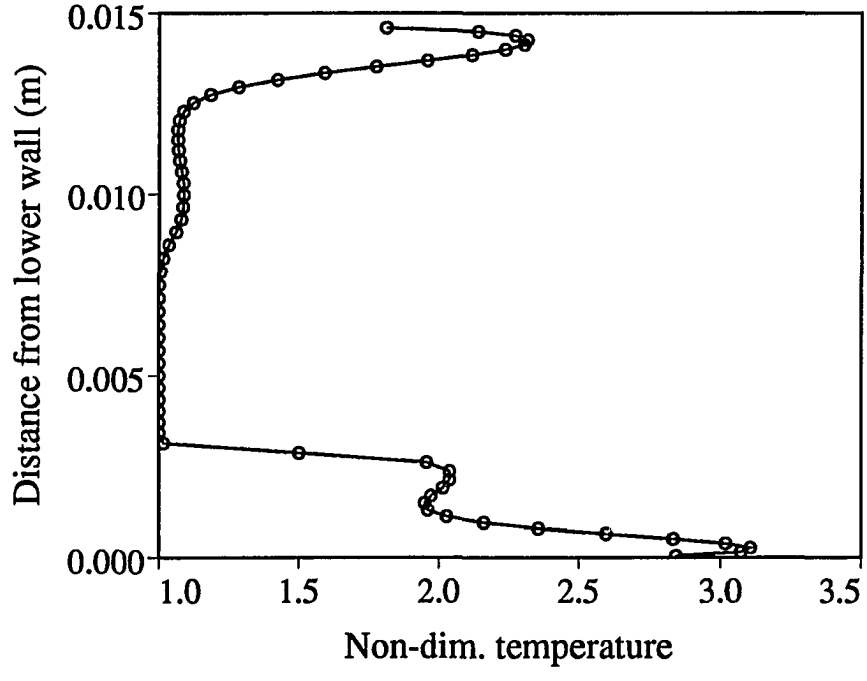


Figure 3.7: Temperature profile at the centerline of the exit plane (x = 3 cm)

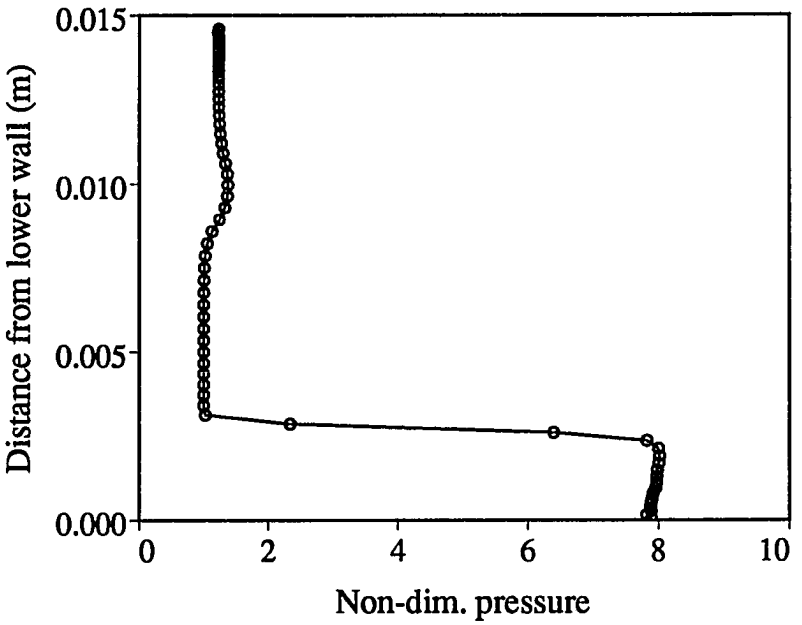


Figure 3.8: Pressure profile at the centerline of the exit plane (x = 3 cm)

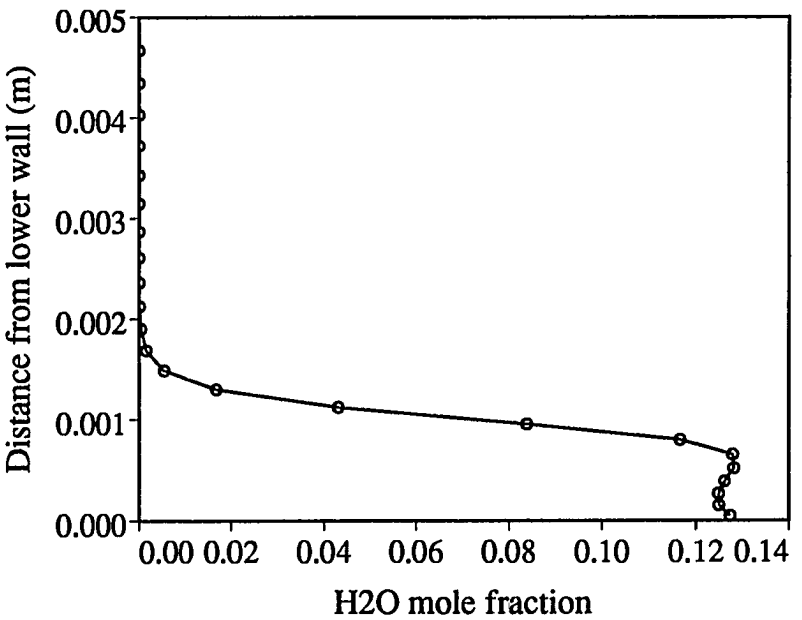


Figure 3.9: Water vapor mole fraction profile at the centerline of the exit plane (x = 3 cm)

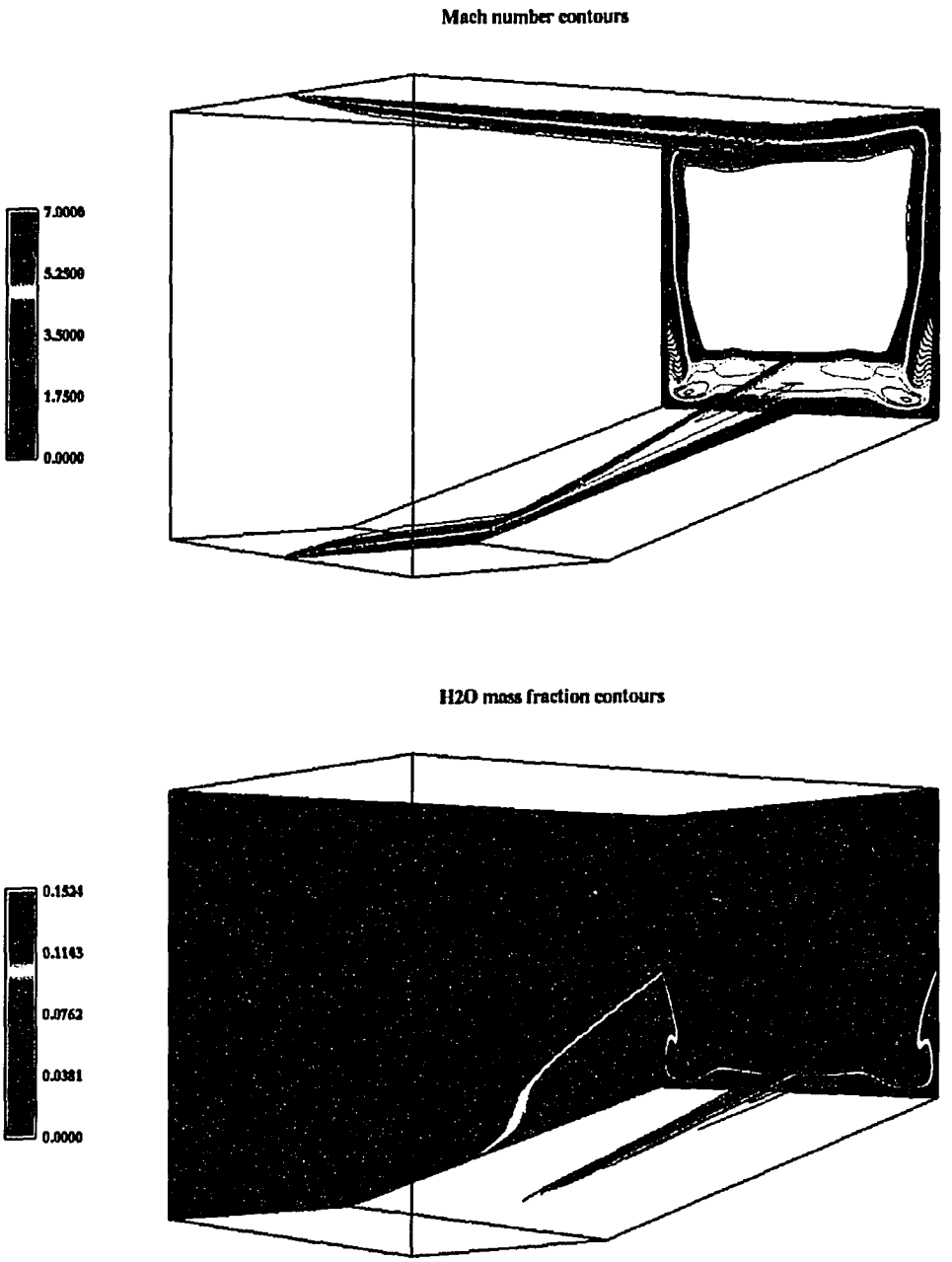


Figure 3.10: Mach number and water vapor mass fraction contours

# CHAPTER 4. TWO-EQUATION TURBULENCE MODELING

Although algebraic turbulence models are well suited for simple wall bounded flows, it is advantageous to use two–equation turbulence models for the corner flows and free–shear layer flows that are encountered in scramjets. In this study, the $k - \epsilon$ turbulence model of Jones–Launder [41] is employed. This model is described in this chapter, as well as the numerical method used to solve the governing equations of the turbulence quantities. Results from four test cases are presented for validation purposes [45]. All aspects of the turbulence model are tested including the high and low Reynolds number form of the turbulence transport equations, and hydrogen–air combustion due to turbulence enhanced mixing. The use of wall functions has been avoided for the sake of generality so that the equations can be directly used to calculate flows past complex geometries. Compressibility corrections [42,43] for modeling compressible mixing layers have been added. Similar to the procedure used for the algebraic turbulence model in the previous chapter, the computed turbulent viscosity is used to calculate the turbulent thermal conductivity and mass diffusivity to account for turbulent mixing. A turbulent Prandtl number ($Pr_t$) of 0.9 is used in all the calculations.

## Turbulence Transport Equations

The vector form of the non–dimensional, steady, low Reynolds number form of the Jones and Launder ($k - \epsilon$) turbulence equations, expressed in generalized coordinates

$(\xi, \eta, \zeta)$, is given by

$$\mathbf{A}_\xi + \mathbf{B}_\eta + \mathbf{C}_\zeta = \mathbf{H} \tag{4.1}$$

where

$$\begin{aligned} \mathbf{A} &= \mathbf{A}_c - \mathbf{A}_d \\ \mathbf{B} &= \mathbf{B}_c - \mathbf{B}_d \\ \mathbf{C} &= \mathbf{C}_c - \mathbf{C}_d \end{aligned} \tag{4.2}$$

In the above equation, the convective fluxes are given by

$$\begin{aligned} \mathbf{A}_c &= \begin{Bmatrix} (\rho \mathbf{U})\, k \\ (\rho \mathbf{U})\, \epsilon \end{Bmatrix} \\ \mathbf{B}_c &= \begin{Bmatrix} (\rho \mathbf{V})\, k \\ (\rho \mathbf{V})\, \epsilon \end{Bmatrix} \\ \mathbf{C}_c &= \begin{Bmatrix} (\rho \mathbf{W})\, k \\ (\rho \mathbf{W})\, \epsilon \end{Bmatrix} \end{aligned} \tag{4.3}$$

where **U**, **V** and **W** are the contravariant velocity components shown below

$$\begin{aligned} \mathbf{U} &= \left(\frac{\xi_x}{J}\right) u + \left(\frac{\xi_y}{J}\right) v + \left(\frac{\xi_z}{J}\right) w \\ \mathbf{V} &= \left(\frac{\eta_x}{J}\right) u + \left(\frac{\eta_y}{J}\right) v + \left(\frac{\eta_z}{J}\right) w \\ \mathbf{W} &= \left(\frac{\zeta_x}{J}\right) u + \left(\frac{\zeta_y}{J}\right) v + \left(\frac{\zeta_z}{J}\right) w \end{aligned} \tag{4.4}$$

and the diffusion fluxes are given by

$$\mathbf{A}_d = \frac{1}{\mathrm{Re}_\infty}\left\{\begin{array}{l}\left(\mu+\frac{\mu_t}{\sigma_k}\right)\left[\left(\frac{\xi_x^2}{J}+\frac{\xi_y^2}{J}+\frac{\xi_z^2}{J}\right)\frac{\partial k}{\partial \xi}+\left(\frac{\xi_x\eta_x}{J}+\frac{\xi_y\eta_y}{J}+\frac{\xi_z\eta_z}{J}\right)\frac{\partial k}{\partial \eta}\right. \\ \qquad\left.+\left(\frac{\xi_x\zeta_x}{J}+\frac{\xi_y\zeta_y}{J}+\frac{\xi_z\zeta_z}{J}\right)\frac{\partial k}{\partial \zeta}\right] \\ \left(\mu+\frac{\mu_t}{\sigma_\epsilon}\right)\left[\left(\frac{\xi_x^2}{J}+\frac{\xi_y^2}{J}+\frac{\xi_z^2}{J}\right)\frac{\partial \epsilon}{\partial \xi}+\left(\frac{\xi_x\eta_x}{J}+\frac{\xi_y\eta_y}{J}+\frac{\xi_z\eta_z}{J}\right)\frac{\partial \epsilon}{\partial \eta}\right. \\ \qquad\left.+\left(\frac{\xi_x\zeta_x}{J}+\frac{\xi_y\zeta_y}{J}+\frac{\xi_z\zeta_z}{J}\right)\frac{\partial \epsilon}{\partial \zeta}\right]\end{array}\right\}$$

$$\mathbf{B}_d = \frac{1}{\mathrm{Re}_\infty}\left\{\begin{array}{l}\left(\mu+\frac{\mu_t}{\sigma_k}\right)\left[\left(\frac{\xi_x\eta_x}{J}+\frac{\xi_y\eta_y}{J}+\frac{\xi_z\eta_z}{J}\right)\frac{\partial k}{\partial \xi}+\left(\frac{\eta_x^2}{J}+\frac{\eta_y^2}{J}+\frac{\eta_z^2}{J}\right)\frac{\partial k}{\partial \eta}\right. \\ \qquad\left.+\left(\frac{\eta_x\zeta_x}{J}+\frac{\eta_y\zeta_y}{J}+\frac{\eta_z\zeta_z}{J}\right)\frac{\partial k}{\partial \zeta}\right] \\ \left(\mu+\frac{\mu_t}{\sigma_\epsilon}\right)\left[\left(\frac{\xi_x\eta_x}{J}+\frac{\xi_y\eta_y}{J}+\frac{\xi_z\eta_z}{J}\right)\frac{\partial \epsilon}{\partial \xi}+\left(\frac{\eta_x^2}{J}+\frac{\eta_y^2}{J}+\frac{\eta_z^2}{J}\right)\frac{\partial \epsilon}{\partial \eta}\right. \\ \qquad\left.+\left(\frac{\eta_x\zeta_x}{J}+\frac{\eta_y\zeta_y}{J}+\frac{\eta_z\zeta_z}{J}\right)\frac{\partial \epsilon}{\partial \zeta}\right]\end{array}\right\} \tag{4.5}$$

$$\mathbf{C}_d = \frac{1}{\mathrm{Re}_\infty}\left\{\begin{array}{l}\left(\mu+\frac{\mu_t}{\sigma_k}\right)\left[\left(\frac{\xi_x\zeta_x}{J}+\frac{\xi_y\zeta_y}{J}+\frac{\xi_z\zeta_z}{J}\right)\frac{\partial k}{\partial \xi}+\left(\frac{\eta_x\zeta_x}{J}+\frac{\eta_y\zeta_y}{J}+\frac{\eta_z\zeta_z}{J}\right)\frac{\partial k}{\partial \eta}\right. \\ \qquad\left.+\left(\frac{\zeta_x^2}{J}+\frac{\zeta_y^2}{J}+\frac{\zeta_z^2}{J}\right)\frac{\partial k}{\partial \zeta}\right] \\ \left(\mu+\frac{\mu_t}{\sigma_\epsilon}\right)\left[\left(\frac{\xi_x\zeta_x}{J}+\frac{\xi_y\zeta_y}{J}+\frac{\xi_z\zeta_z}{J}\right)\frac{\partial \epsilon}{\partial \xi}+\left(\frac{\eta_x\zeta_x}{J}+\frac{\eta_y\zeta_y}{J}+\frac{\eta_z\zeta_z}{J}\right)\frac{\partial \epsilon}{\partial \eta}\right. \\ \qquad\left.+\left(\frac{\zeta_x^2}{J}+\frac{\zeta_y^2}{J}+\frac{\zeta_z^2}{J}\right)\frac{\partial \epsilon}{\partial \zeta}\right]\end{array}\right\}$$

The source vector is given by

$$\mathbf{H} = \frac{1}{J}\left\{\begin{array}{c} P-\rho\epsilon-\frac{2\mu}{\mathrm{Re}_\infty}\left(\frac{\partial\sqrt{k}}{\partial \bar{n}}\right)^2+C_k \\ C_1\frac{\epsilon}{k}P+\frac{2\mu\mu_t}{\rho\mathrm{Re}_\infty^2}\left(\frac{\partial^2 u}{\partial \bar{n}^2}\right)^2-C_2 f_2\frac{\rho\epsilon^2}{k}\end{array}\right\} \tag{4.6}$$

where $C_k$ is the compressibility term [42,43], $P$ is the production term which in non-dimensional, tensor notation is given by

$$P = \frac{\mu_t}{\mathrm{Re}_\infty}\left(u_{i,j}+u_{j,i}-\frac{2}{3}\delta_{ij}u_{k,k}\right)u_{i,j}-\frac{2}{3}\rho k u_{k,k} \tag{4.7}$$

and $\bar{n}$ is the direction normal to the wall.

In the preceding equations, the turbulence quantities have been non-dimensionalized as follows

$$\mu_t = \frac{\mu_t^*}{\mu_\infty^*}, \qquad k = \frac{k^*}{V_\infty^{*2}}, \qquad \epsilon = \frac{\epsilon^* L^*}{V_\infty^{*3}}$$

The model constants appearing in Eqs. 4.5 and 4.6 are set as follows

$$\sigma_k = 1.0, \qquad \sigma_\epsilon = 1.3, \qquad C_1 = 1.44, \qquad C_2 = 1.92 \tag{4.8}$$

and

$$f_2 = 1 - 0.3\exp\left(-\mathrm{R}_t^2\right) \tag{4.9}$$

where $\mathrm{R}_t$ is the turbulent Reynolds number given in non-dimensional form by

$$\mathrm{R}_t = \mathrm{Re}_\infty \frac{\rho k^2}{\mu \epsilon} \tag{4.10}$$

The turbulent viscosity appearing in the above equations is given by

$$\mu_t = \mathrm{Re}_\infty \left(\rho C_\mu f_\mu \frac{k^2}{\epsilon}\right) \tag{4.11}$$

where

$$C_\mu = 0.09 \qquad \text{and} \qquad f_\mu = \exp\left(\frac{-2.5}{1 + 0.02\mathrm{R}_t}\right) \tag{4.12}$$

The above form of the steady, turbulence transport equations are simplified by making the parabolizing assumption of dropping the streamwise diffusion terms. This facilitates the streamwise marching of these equations in a manner similar to the approach used for the fluid flow equations. Thus the final form of the $k - \epsilon$ turbulence equations becomes

$$\underbrace{(\mathbf{A}_c)_\xi + (\mathbf{B}_c)_\eta + (\mathbf{C}_c)_\zeta}_{Convective\ terms} - \underbrace{(\mathbf{B}_d^*)_\eta - (\mathbf{C}_d^*)_\zeta}_{Diffusion\ terms} = \underbrace{\mathbf{H}}_{Source\ term} \tag{4.13}$$

In the preceding equation the convective fluxes ($\mathbf{A}_c$, $\mathbf{B}_c$, $\mathbf{C}_c$) and the source term ($\mathbf{H}$) are of the same form as shown in Eqs. 4.3 and 4.6, respectively. The parabolized diffusion fluxes are now of the form

$$\mathbf{B}_d^* = \left\{ \left( A_{\eta\eta_k} \frac{\partial k}{\partial \eta} + A_{\eta\zeta_k} \frac{\partial k}{\partial \zeta} \right), \left( A_{\eta\eta_\epsilon} \frac{\partial \epsilon}{\partial \eta} + A_{\eta\zeta_\epsilon} \frac{\partial \epsilon}{\partial \zeta} \right) \right\}^T \tag{4.14}$$

$$\mathbf{C}_d^* = \left\{ \left( A_{\zeta\eta_k} \frac{\partial k}{\partial \eta} + A_{\zeta\zeta_k} \frac{\partial k}{\partial \zeta} \right), \left( A_{\zeta\eta_\epsilon} \frac{\partial \epsilon}{\partial \eta} + A_{\zeta\zeta_\epsilon} \frac{\partial \epsilon}{\partial \zeta} \right) \right\}^T \tag{4.15}$$

where

$$\begin{aligned}
A_{\eta\eta_k} &= \frac{1}{\mathrm{Re}_\infty} \left( \mu + \frac{\mu_t}{\sigma_k} \right) \left( \frac{\eta_x^2}{J} + \frac{\eta_y^2}{J} + \frac{\eta_z^2}{J} \right) \\
A_{\zeta\zeta_k} &= \frac{1}{\mathrm{Re}_\infty} \left( \mu + \frac{\mu_t}{\sigma_k} \right) \left( \frac{\zeta_x^2}{J} + \frac{\zeta_y^2}{J} + \frac{\zeta_z^2}{J} \right) \\
A_{\zeta\eta_k} = A_{\eta\zeta_k} &= \frac{1}{\mathrm{Re}_\infty} \left( \mu + \frac{\mu_t}{\sigma_k} \right) \left( \frac{\eta_x \zeta_x}{J} + \frac{\eta_y \zeta_y}{J} + \frac{\eta_z \zeta_z}{J} \right) \\
A_{\eta\eta_\epsilon} &= \frac{1}{\mathrm{Re}_\infty} \left( \mu + \frac{\mu_t}{\sigma_\epsilon} \right) \left( \frac{\eta_x^2}{J} + \frac{\eta_y^2}{J} + \frac{\eta_z^2}{J} \right) \\
A_{\zeta\zeta_\epsilon} &= \frac{1}{\mathrm{Re}_\infty} \left( \mu + \frac{\mu_t}{\sigma_\epsilon} \right) \left( \frac{\zeta_x^2}{J} + \frac{\zeta_y^2}{J} + \frac{\zeta_z^2}{J} \right) \\
A_{\zeta\eta_\epsilon} = A_{\eta\zeta_\epsilon} &= \frac{1}{\mathrm{Re}_\infty} \left( \mu + \frac{\mu_t}{\sigma_\epsilon} \right) \left( \frac{\eta_x \zeta_x}{J} + \frac{\eta_y \zeta_y}{J} + \frac{\eta_z \zeta_z}{J} \right)
\end{aligned} \tag{4.16}$$

At a solid wall boundary, both $k$ and $\epsilon$ are zero.

## Numerical Method

The turbulence transport equations are solved uncoupled from the fluids. Hence fluid fluxes (the coefficients of the convective terms) are known quantities from the most recent fluid integration step. This permits the turbulence equations to remain in strong conservation-law form and thus they can be solved by using a finite–volume formulation. The convective terms are modeled using an upwind–biased TVD (Total Variation Diminishing) scheme, similar to the fluid dynamic equations. The user has the option of choosing

a first–order, second–order, or third–order accurate upwind scheme. The diffusion and source terms are modeled using second–order central differences with the source term lagged to the $n$th marching station. This results in the decoupling of the $k$ and $\epsilon$ equations. The resulting set of algebraic equations is cast into a tridiagonal format and solved in an iterative manner by using a line Gauss–Seidel procedure with successive over–relaxation (SOR). The iterations are continued until the residual drops below a specified tolerance level $\epsilon$. The residual is defined as

$$\mid r^{i+1} - r^{i} \mid \leq \epsilon$$

where $i+1$ and $i$ are the current and previous iteration levels, respectively, and $r$ denotes the turbulence quantity, $k$ or $\epsilon$.

In the space marching mode, the low Reynolds number form of the $k-\epsilon$ turbulence model requires smaller step sizes to overcome the stiffness introduced by the near wall terms. In addition, successful simulations require suitable initial conditions for the turbulence quantities, $k$ and $\epsilon$.

## Numerical Results and Discussion

Four test cases are used to validate the new code with the $k-\epsilon$ turbulence model. These test cases are indicative of the flows encountered in the scramjet engine of a hypersonic vehicle. The first test case is the 2–D supersonic free–shear layer calculation of Viegas *et al.* [46]. The second test case is a supersonic, perfect gas, 2–D flat plate boundary layer. The third test case is the Burrows–Kurkov supersonic combustion experiment [44] described previously. The fourth test case resulted from the lack of fully documented experimental data for supersonic, hydrogen–air combustion cases for validation of CFD codes. This numerical experiment consists of a supersonic, combusting, free-shear layer [48].

Test case I

This test case consists of a 2–D, compressible, free–shear layer. Two parallel supersonic streams of perfect gas are initially separated by a splitter plate with no boundary layer thickness as shown in Fig. 4.1. The upper layer is taken to be the high speed layer. This test case was chosen to validate the high Reynolds number form of the Jones–Launder turbulence model [41] and hence all the low Reynolds number terms were neglected. The flow conditions were taken to be the same as that used by Viegas *et al.* [46]. Both streams had the same total temperature and static pressure of 833.33 K and 1 atm., respectively. The Mach numbers of the two streams were 4.92 and 1.1. No compressibility corrections were used in this calculation.

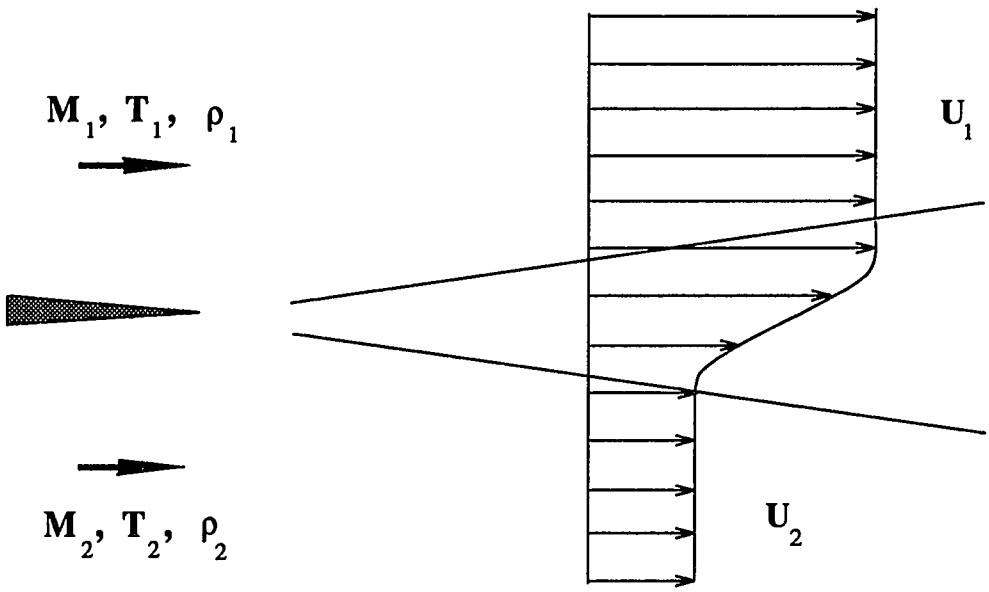


Figure 4.1: Schematic of the free–shear layer

The present results are compared with the Navier–Stokes calculation of Viegas *et al.* The grid used in this calculation was clustered at the shear–layer and consisted of 51 points in the normal direction. The shear layer growth rate is shown in Fig. 4.2. The vorticity thickness is defined as

$$dw = \frac{(U_1 - U_2)}{\left(\frac{\partial U}{\partial y}\right)_{max}} \tag{4.17}$$

The computed shear layer growth rate is linear and in excellent agreement with that of Viegas *et al.* as seen in Fig. 4.2.

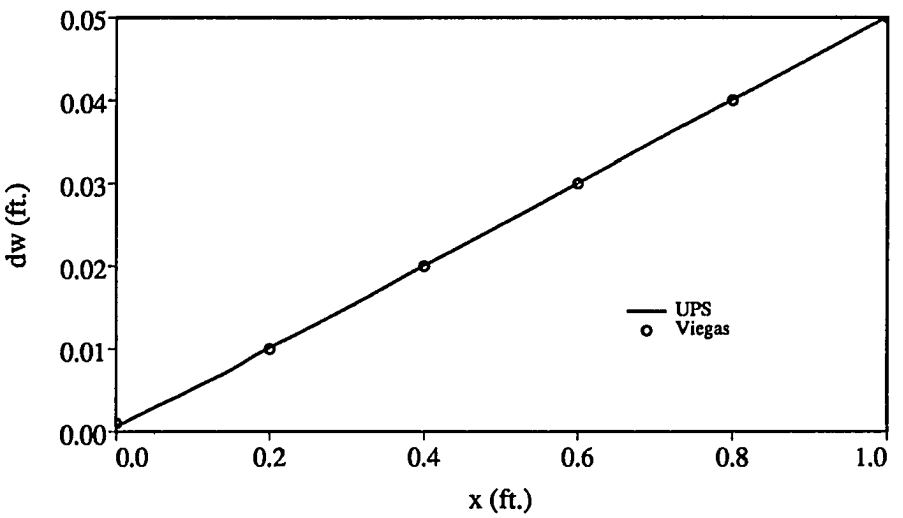


Figure 4.2: Comparison of the shear layer growth rate for the free–shear layer

The turbulence kinetic energy and velocity profiles, at various streamwise locations are plotted against the normalized distance across the shear layer in Figs. 4.3 and 4.4, respectively. The distance is normalized with respect to the local vorticity thickness, $dw$. Two flow phenomena are worth noting:

1. The turbulence kinetic energy and velocity profiles become self–similar at down-

stream locations.

2. Both the shear layer and high speed layer tend to turn towards the low speed layer.

Similar observations were reported by Viegas *et al.* The slight upper shift in the velocity profiles is attributed to the differences in the far field boundary conditions imposed. The computed results are in good agreement with the results of Viegas *et al.*

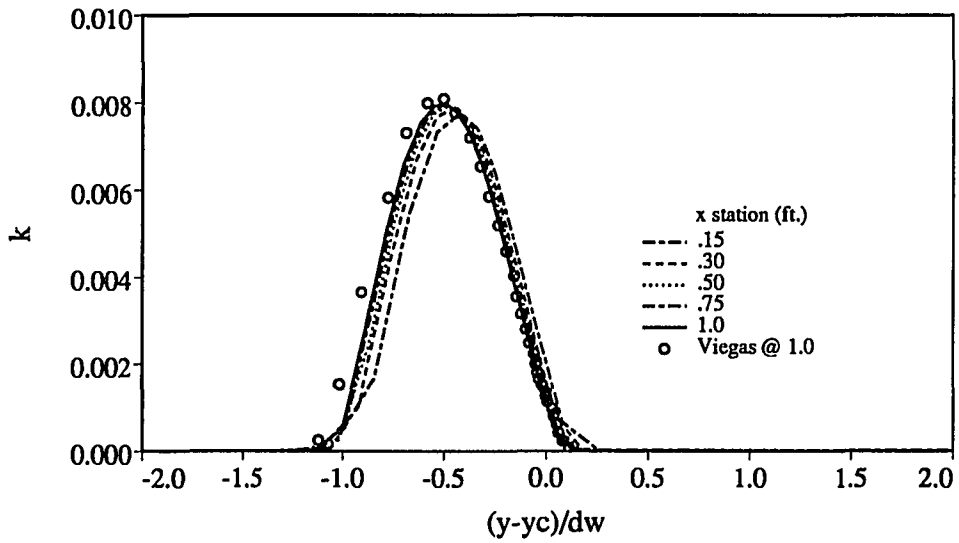


Figure 4.3: Comparison of the non-dimensional turbulent kinetic energy profiles for the free–shear layer

**Test case II**

This test case consists of a turbulent boundary layer on a 2–D flat plate in supersonic ($M_\infty = 5$) flow as shown in Fig. 4.5. This test case serves to validate the low Reynolds number form of the Jones–Launder turbulence model. No compressibility corrections were used and an adiabatic wall boundary condition was imposed.

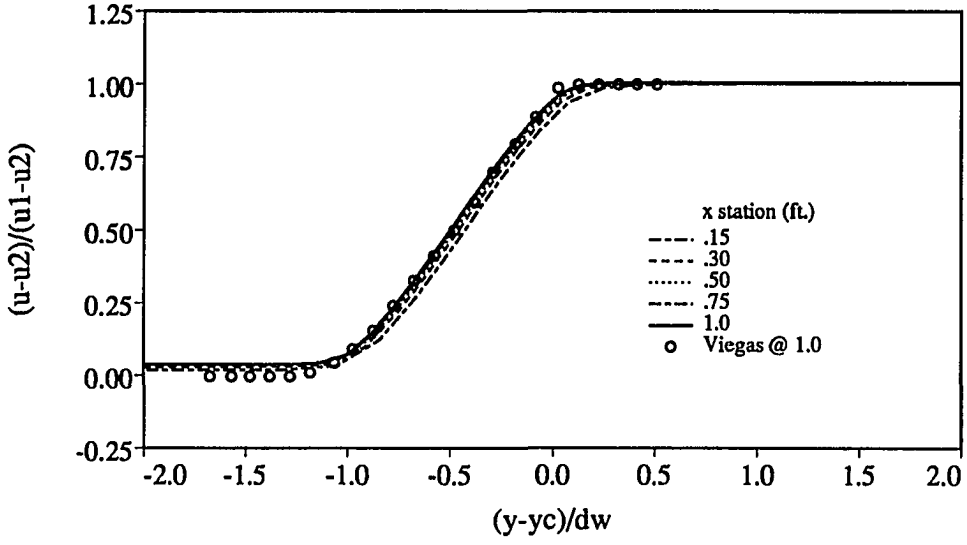


Figure 4.4: Comparison of the U–velocity profiles for the free–shear layer

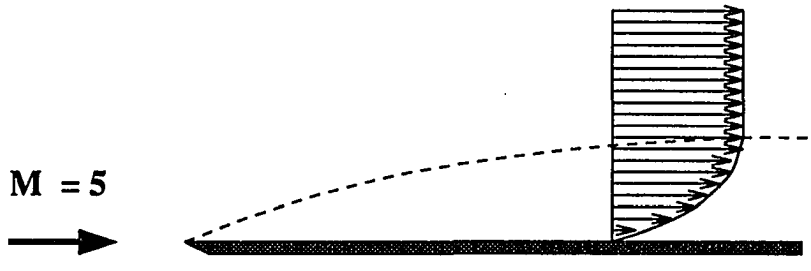


Figure 4.5: Schematic of a flat plate in supersonic flow

The grid was clustered at the wall to resolve the boundary layer and 60 grid points were employed in the normal direction. The maximum value of $y^+$ at the first point off the wall was 0.7. To obtain a starting profile for the turbulence quantities $k$ and $\epsilon$, the algebraic model of Baldwin–Lomax [39] was employed for the first 500 steps (0.45 cm). Using this solution and assuming the turbulence to be in equilibrium, $\epsilon$ was set equal to the ratio of the production of the turbulence kinetic energy $P$ and the density $\rho$:

$$\epsilon = \frac{P}{\rho} \tag{4.18}$$

The values for $k$ were then obtained from Eq. 4.11 assuming $f_\mu$ as unity:

$$k = \sqrt{\frac{\mu_t \epsilon}{\mathrm{Re}_\infty \rho C_\mu}} \tag{4.19}$$

The results of the streamwise variation of the local skin friction coefficient are compared with the results obtained from the Baldwin–Lomax turbulence model and the Van Driest II theory [47] in Fig. 4.6. The mean streamwise velocity profile, using inner wall variables $u^+$ and $y^+$, at a downstream station of x = 0.1 m is compared with that obtained from a Baldwin–Lomax turbulence model in Fig. 4.7. The results are in good agreement.

Test case III

The two–dimensional Burrows–Kurkov experiment [44] described earlier was chosen for one turbulent combustion validation. In this experiment, combustion occurs in the supersonic shear layer produced by the injection of hydrogen into a stream of vitiated air. The schematic of the experimental setup was shown previously in Fig. 3.2 and the freestream conditions for the hydrogen jet and the vitiated air were given in Table 3.1. The inlet temperature and velocity profiles, provided by the experimentalists (Fig. 4.8), were used to generate the inlet flow conditions. The first 2 cm of the flow at the inlet

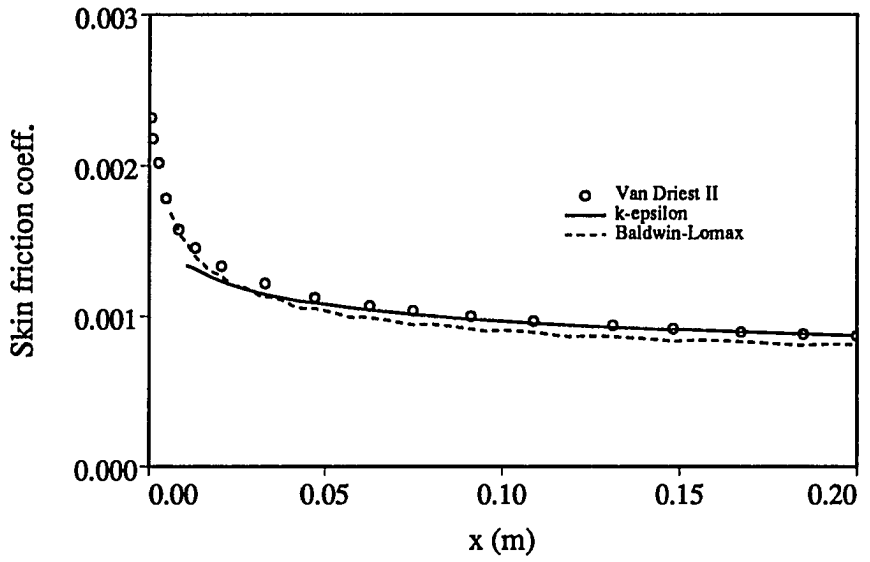


Figure 4.6: Comparison of the local skin friction coefficient for a flat plate in supersonic flow ($M_\infty = 5$)

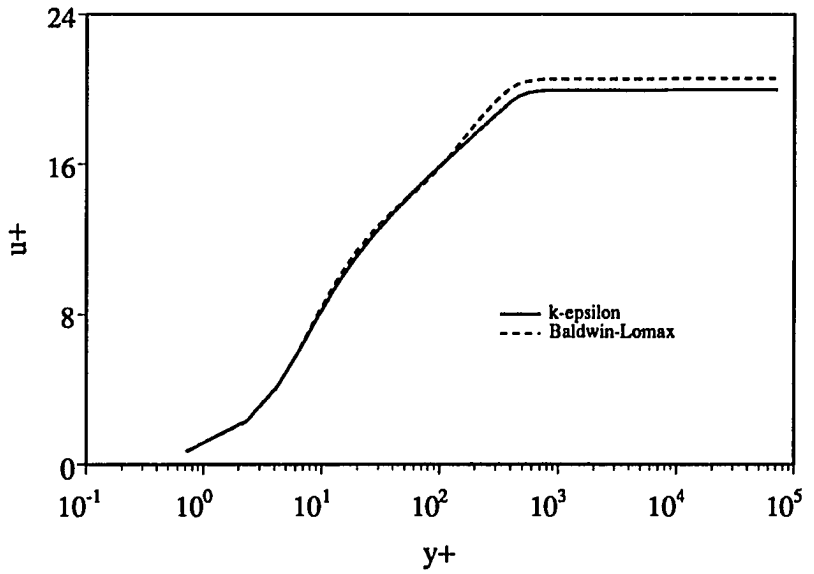


Figure 4.7: Comparison of the streamwise velocity profiles for a flat plate in supersonic flow ($M_\infty = 5$) at x = 0.1 m

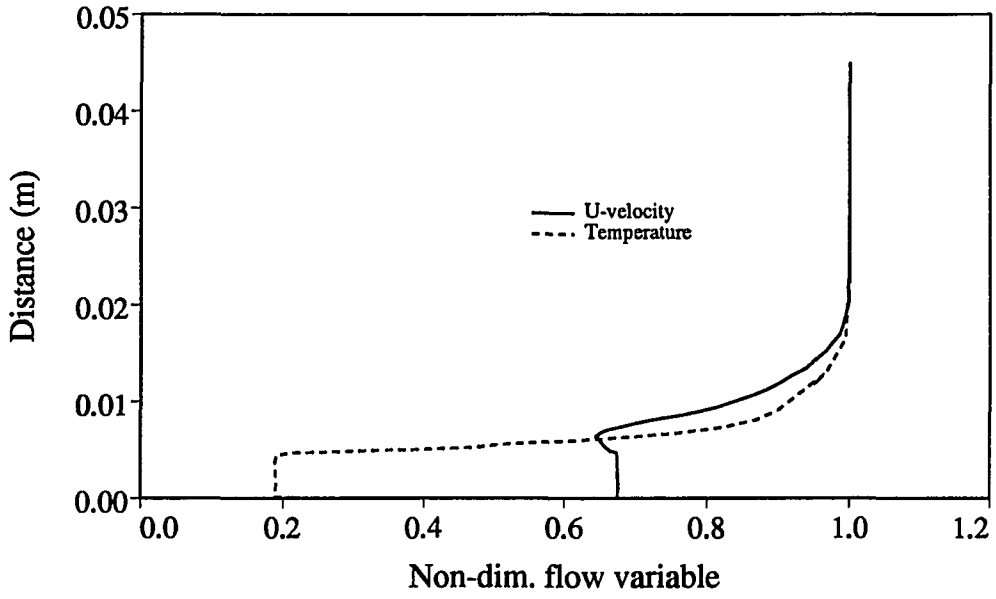


Figure 4.8: Initial profiles at x = 0 of U-velocity and temperature for the Burrows–Kurkov experiment

were computed using the Baldwin–Lomax turbulence model [39]. As in the previous test case, this provided $k$ and $\epsilon$ profiles to initiate the $k - \epsilon$ calculations. The low Reynolds number form of the turbulence equations were used along with the Zeman compressibility correction [42].

A grid consisting of 150 points in the normal direction was clustered at both walls. The first point off the wall was placed at $1 \times 10^{-7}$ m. The computed species mole fraction profiles of $H_2$, $H_2O$, and $O_2$ at the exit plane (x = 35.6 cm) are compared with the experimental profiles in Fig. 4.9. The diffusion of hydrogen away from the lower wall and the width of the flame, indicated by the water vapor profile, at the exit plane are greater for the $k - \epsilon$ turbulence model than for the Baldwin–Lomax model shown in the previous

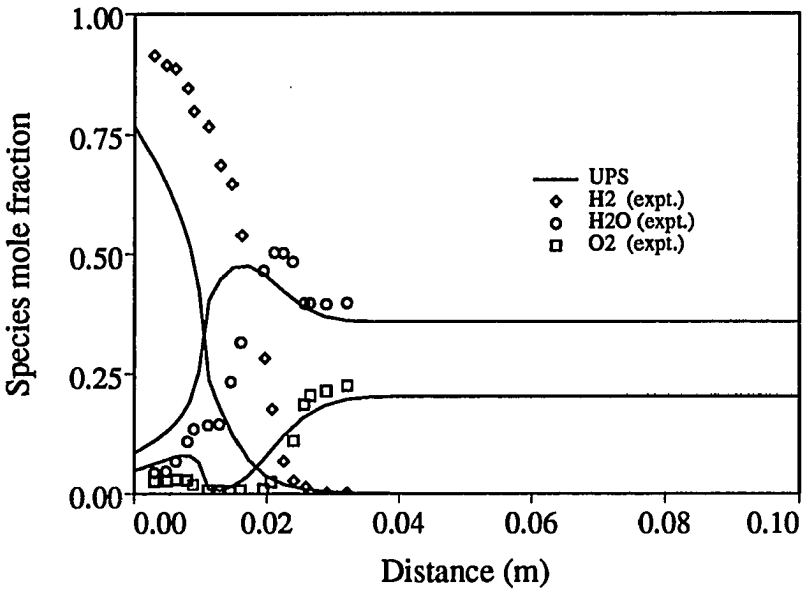


Figure 4.9: Comparison of species mole fraction profiles at the exit plane (x = 35.6 cm) for the Burrows–Kurkov experiment

chapter. As observed for the Baldwin–Lomax model, the location of the flame and the peaks in the species profiles are closer to the wall than the experimental data. In this test case the combustion is dominated by turbulent mixing and the difference in results is attributed to the lack of knowledge of the freestream turbulence that prevailed during the experiment. Similar results have been obtained by other investigators using the Baldwin–Lomax turbulence model [14,25] and the $k - \epsilon$ turbulence model [59]. Figure 4.10 shows the comparison between the computed and the experimental profiles of the total temperature at the exit plane (x = 35.6 cm). The peak in the total temperature profile was found to be slightly lower than that reported by the experimentalists. The main difference in the two models is in the accuracy of the prediction of the ignition location. Ignition based on the concentration of OH occurred at about 25.2 cm for the $k - \epsilon$ model. This is in excellent agreement with the experimental result of 25.1 cm. The Baldwin-Lomax turbulence model

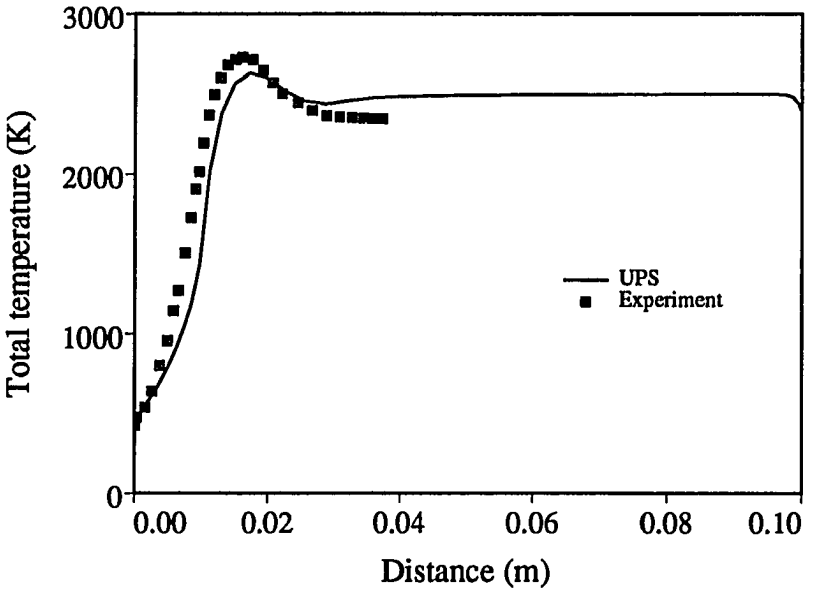


Figure 4.10: Comparison of total temperature profiles at the exit plane (x = 35.6 cm) for the Burrows–Kurkov experiment

predicted ignition at about 15 cm.

Test case IV

The fourth test case is a numerical experiment [48] that was devised to provide a simple geometry and remove the uncertainty in the freestream turbulence that is inherent in most hydrogen–air combustion experiments. This case consists of two supersonic, parallel streams of air of different chemical compositions, at atmospheric pressure, separated by a splitter plate. The schematic of this case is similar to that of Test case I as shown in Fig. 4.1. The chemical composition of the two layers is given in Table 4.1.

The two layers are both 2.5 cm thick. The initial profiles at x = 0, of velocity, temperature, and $k$ and $\epsilon$ are shown in Figs. 4.11 and 4.12, respectively. A grid of 71 points in the normal direction was used with clustering at the shear layer interface. The

Table 4.1: Chemical composition of Test case IV

| Layer | Mass fraction | | |
|---|---|---|---|
| | $H_2$ | $O_2$ | $N_2$ |
| Upper | 0.1 | 0.0 | 0.9 |
| Lower | 0.0 | 0.237 | 0.763 |

high Reynolds number form of the turbulence equations were used along with the Zeman compressibility correction [42]. Calculations were carried out to 20 cm downstream of the starting plane where the profiles were compared with the results obtained from the STUFF code [11], which solves the chemistry and turbulence equations in a fully coupled manner. The turbulence enhanced mixing in the free–shear layer causes combustion. The ignition was found to occur at about 2.5 cm as shown by the OH and $H_2O$ mass fraction contours in Fig. 4.13. Results from the two codes for the location of the ignition point agreed well. Figures 4.14 – 4.16 show the comparison between the UPS and the STUFF results for species mass fractions, temperature, velocity, and $k$ and $\epsilon$ profiles at x = 20 cm, respectively. The results are in good agreement. It should be noted that at the last streamwise station (x = 20 cm) there were about 20 grid points in the shear layer. The calculations using the STUFF code were performed on an identical grid, with the same initial conditions and the same turbulence model as the UPS code.

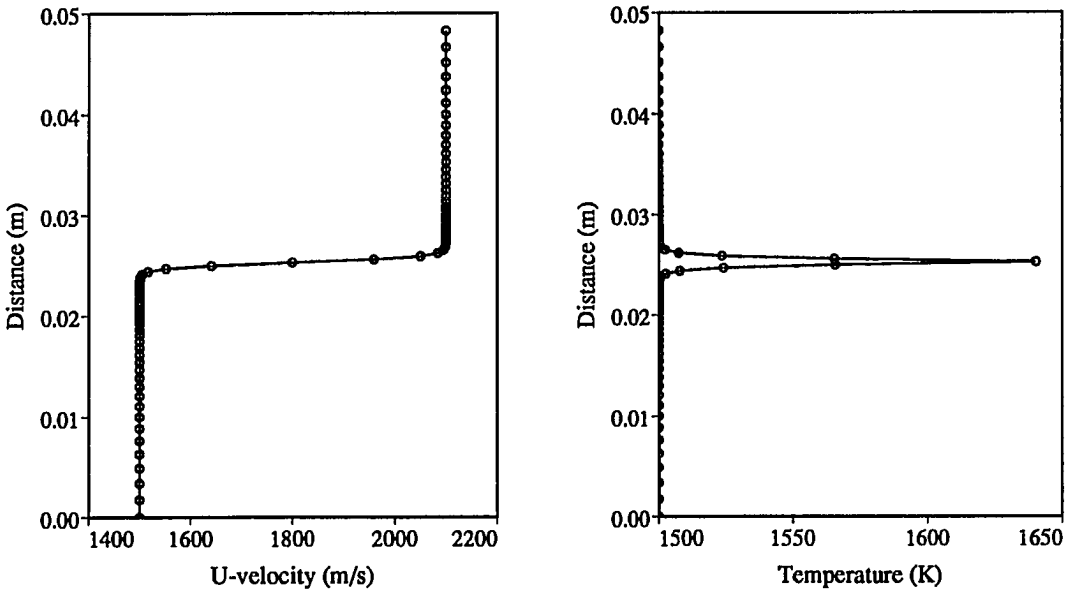


Figure 4.11: Initial profiles of U-velocity and temperature at x = 0 for the supersonic, combusting, free–shear layer

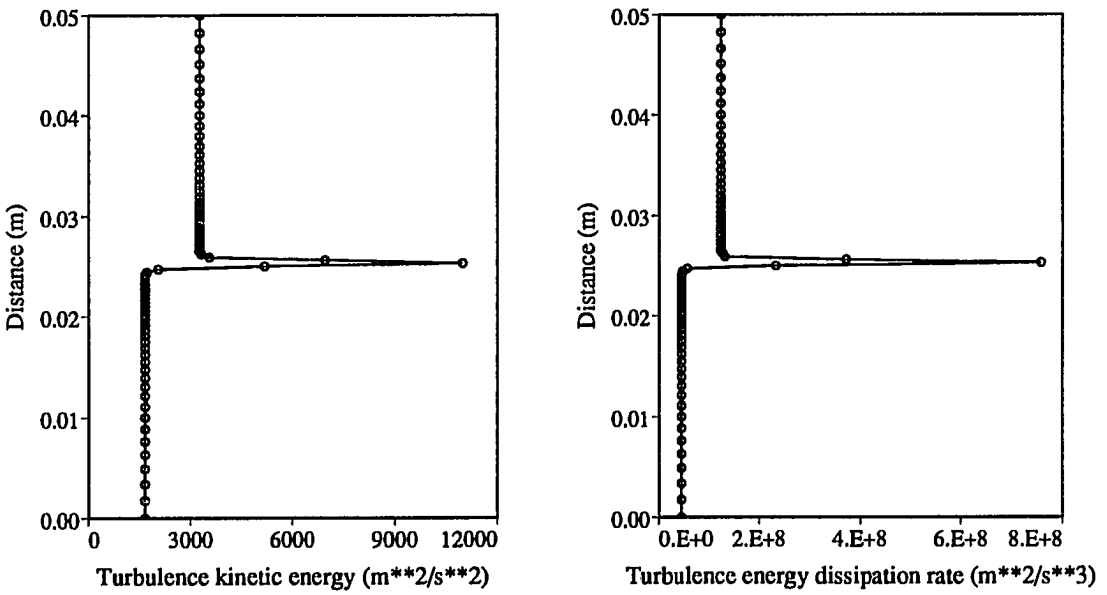


Figure 4.12: Initial profiles of turbulence kinetic energy and turbulence energy dissipation rate at x = 0 for the supersonic, combusting, free–shear layer

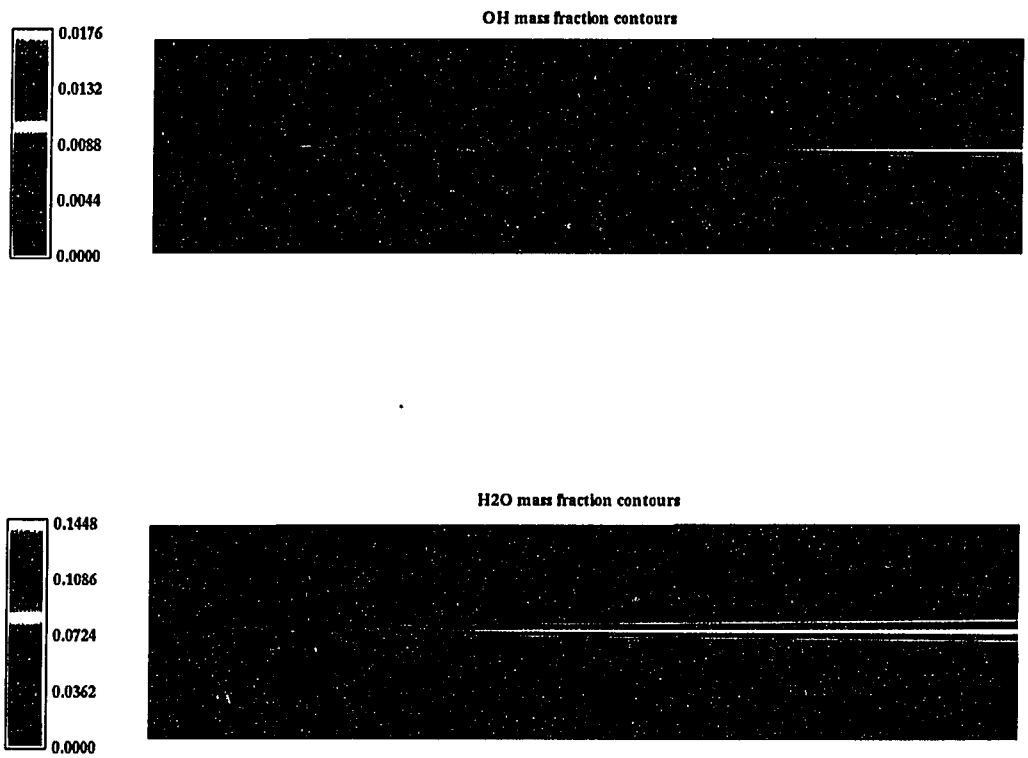


Figure 4.13: Ignition point as indicated by the OH and $H_2O$ mass fraction contours

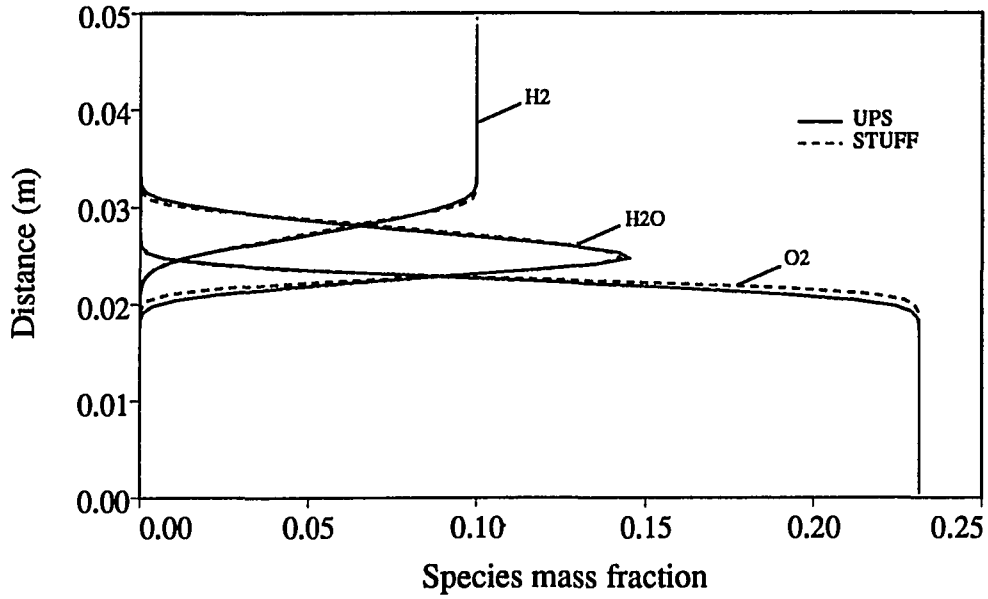


Figure 4.14: Comparison of species mass fraction profiles at x = 20 cm for the supersonic, combusting, free–shear layer

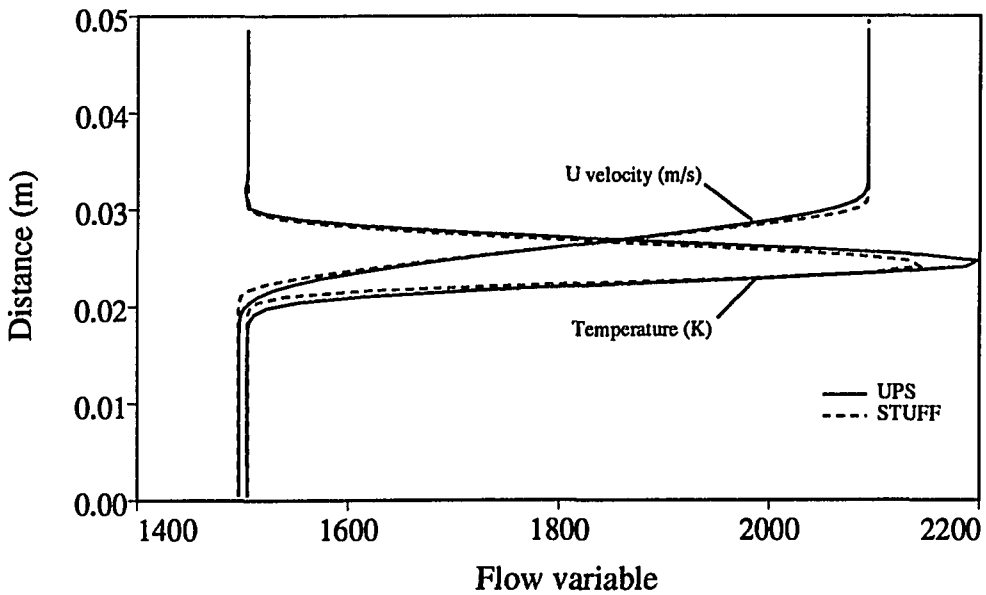


Figure 4.15: Comparison of U-velocity and temperature profiles at x = 20 cm for the supersonic, combusting, free–shear layer

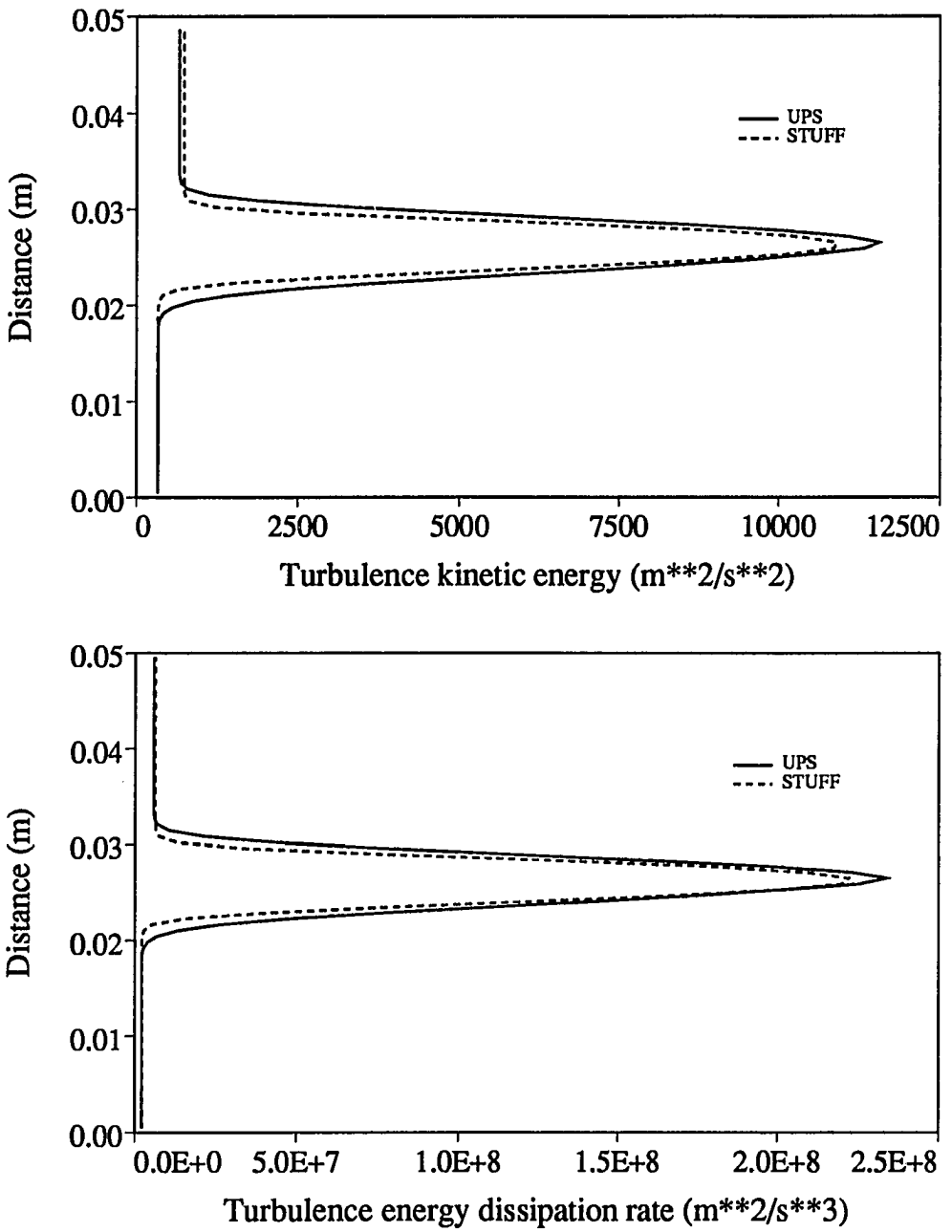


Figure 4.16: Comparison of turbulence kinetic energy, and turbulence energy dissipation rate profiles at x = 20 cm for the supersonic, combusting, free–shear layer

# CHAPTER 5. GENERIC HYPERSONIC SPACE-PLANE COMPUTATIONS

The main focus of this chapter is to demonstrate the capability of the new UPS code to efficiently solve the three–dimensional, tip–to–tail, integrated aerodynamic and propulsive flowfields of a generic hypersonic space plane and to study the flow structure around such a configuration. The air around the space plane is assumed to be in chemical nonequilibrium.

## Numerical Results and Discussion

The generic hypersonic space plane configuration chosen in this study is the Test Technology Demonstrator (TTD). The TTD geometry is shown in Fig. 5.1. The 3–D exterior grid consisted of three zones as shown in Fig. 5.2. The details of the grids are given in Table 5.1. Owing to the symmetry of the configuration, the calculations were performed on one half the cross–section only. The freestream conditions correspond to an altitude of 100,000 feet (30.5 km), a Mach number of 10.05 and a Reynolds number of $3.512429 \times 10^6$ /m. The freestream temperature was taken to be 227 K and the wall temperature was held constant at 1000 K. As is shown later, these conditions provide a shock–on–lip condition at the inlet of the scramjet which is the optimum operating condition.

The starting solution at the nose was obtained by using a conical stepback procedure [60]. It was found that a sharp nose cone, with its apex at the origin, blended well with the given forebody shape without causing any abrupt expansion or compression corners.

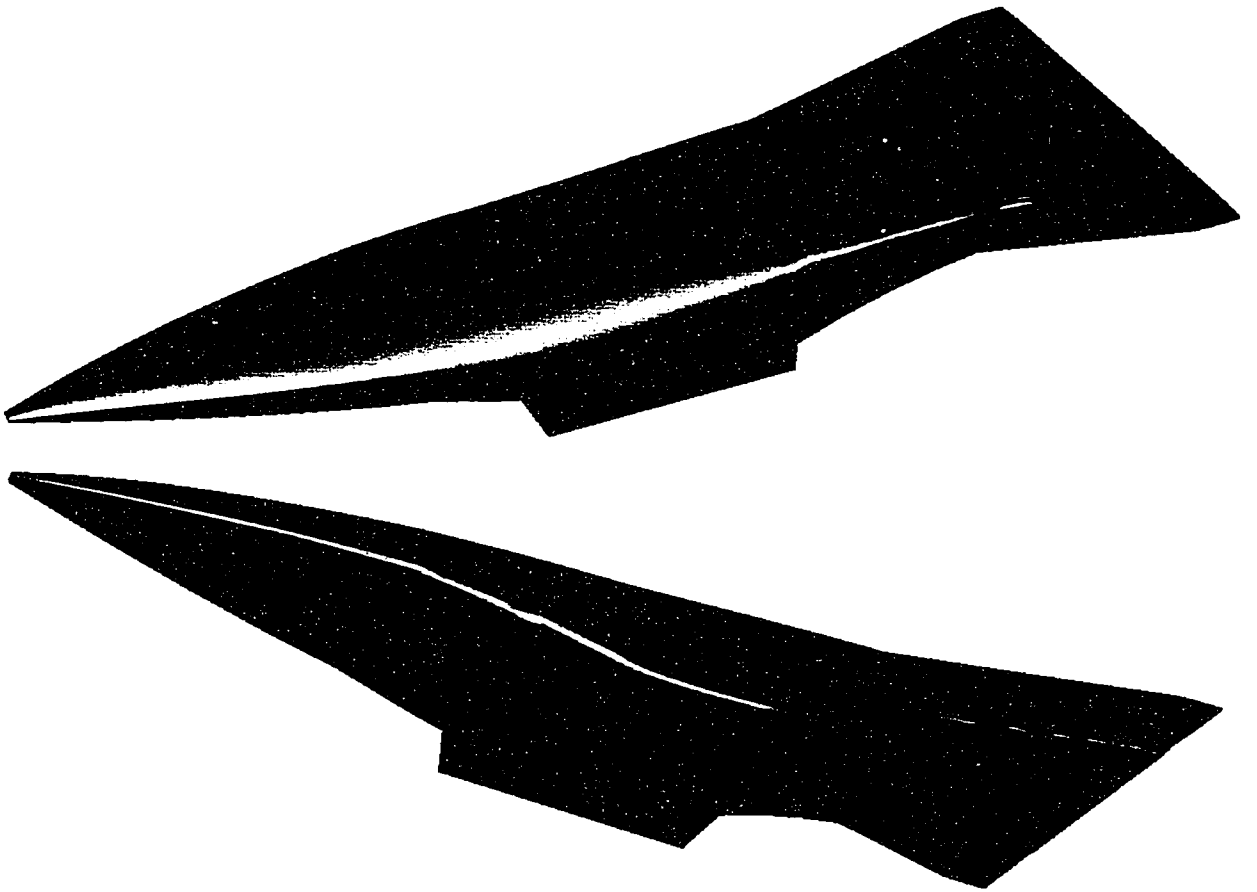

Figure 5.1: Perspective views of the Test Technology Demonstrator (TTD) geometry

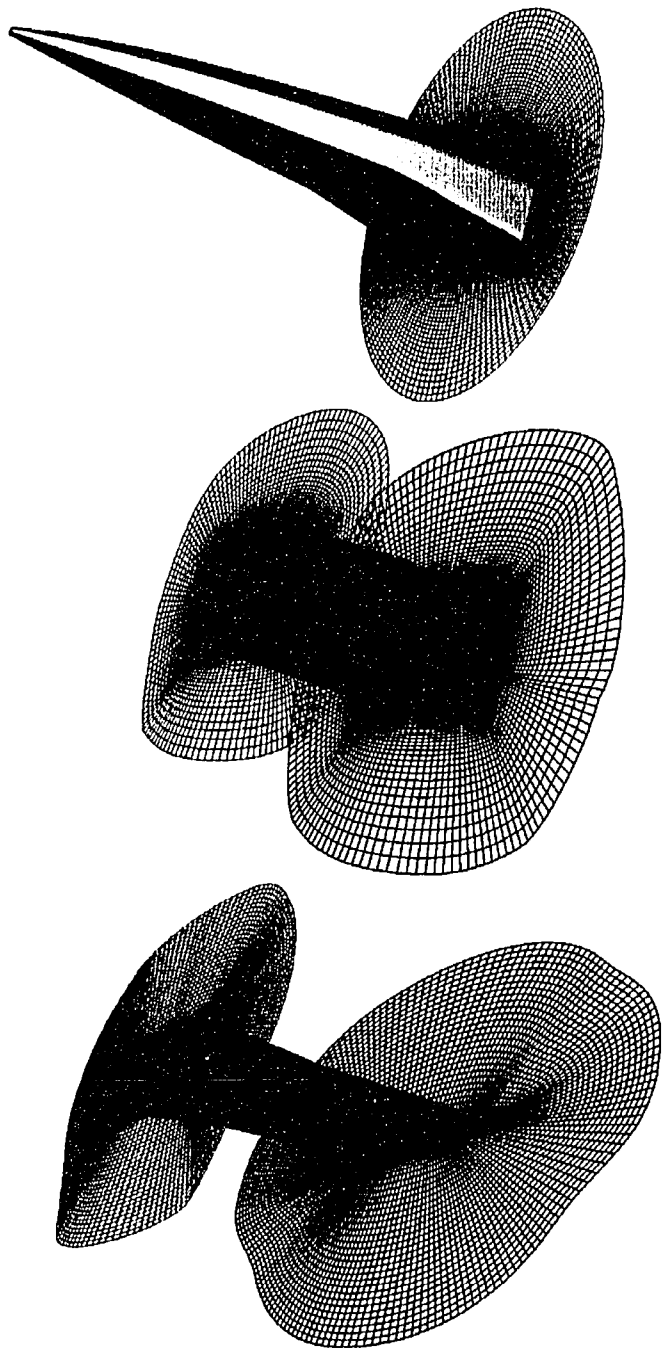

Figure 5.2: TTD grids: forebody, midsection and aftbody

Table 5.1: Grid topology of the TTD geometry[a]

| Zone | x-location (m) | | Number of planes in each direction | | |
|---|---|---|---|---|---|
| | Starting | Ending | Streamwise | Crossflow | Normal |
| Forebody | 0.0127127 | 0.368300 | 31 | 65 | 65 |
| Midsection | 0.3555910 | 0.546113 | 16 | 75 | 50 |
| Engine | 0.3556000 | 0.546100 | 16 | 40 | 82 |
| Aftbody | 0.5354830 | 0.850905 | 26 | 85 | 50 |

[a]The forebody, midsection and engine grids are coincident in the crossflow plane at x = 0.3683 m.

The stepback procedure took 1200 steps to converge producing a well defined bow shock at the nose. This is depicted in Fig. 5.3 by the pressure contours in the crossflow plane at the nose. With this starting solution, two test cases were then computed as described below. The Baldwin–Lomax turbulence model [39,40] was used for both cases.

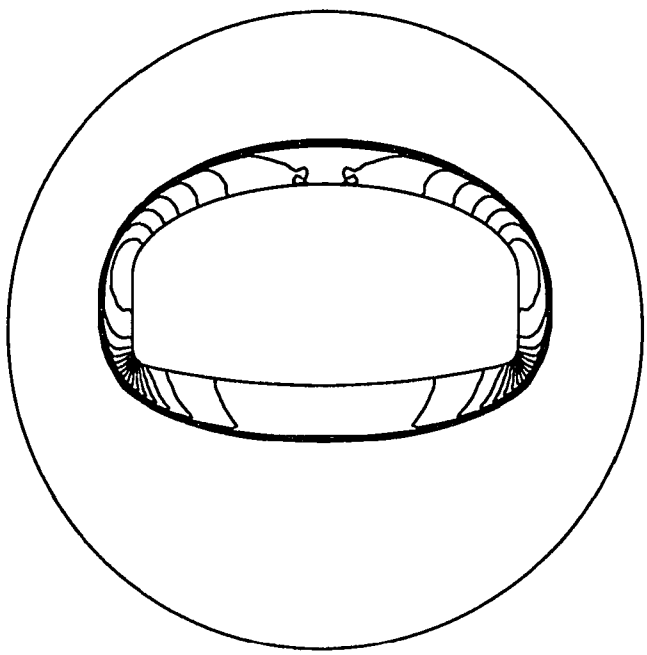

Figure 5.3: Converged stepback solution at the nose (pressure contours)

**Test case I**

This test case simulates a power-off flight condition. The air surrounding the TTD configuration was assumed to be in chemical nonequilibrium. For the forebody calculations, smaller step sizes were taken in the vicinity of the compression corner (x = 0.26938 m) to properly capture the emanating shock.

Figure 5.4 shows the crossflow plane at the inlet of the scramjet where the forebody grid (in black) ends and the midsection grid (in red) begins. For the sake of clarity, only the first (body surface) and the last circumferential grid lines are shown along with the radial grid lines for the midsection grid. As can be seen, the chosen flow conditions result in a shock–on–lip condition and the shock generated by the forebody compression corner enters the scramjet.

The solution at the end of the forebody zone is transferred over to the new grid of the midsection zone by using a 2–D interpolation procedure. The original and interpolated Q–vectors are shown in Fig. 5.5. The Q–vector is the vector of conserved variables that is computed in the fluid dynamics numerical algorithm and is given by

$$\mathrm{Q} = \{\rho, \rho u, \rho v, \rho w, E_t\}^T$$

A similar procedure was employed to obtain the starting solution for the internal flow inside the scramjet and at the exit plane of the scramjet where the solution from the two independent grid zones, one corresponding to the internal flow in the scramjet and one to the external flow over the midsection, were interpolated onto the single grid zone corresponding to the aftbody of the TTD.

The shock originating from the forebody compression corner enters the scramjet engine and reflects back and forth between the top and bottom walls of the engine. Also, the bow shock hits the cowl lip and reflects, and interacts with the forebody compression

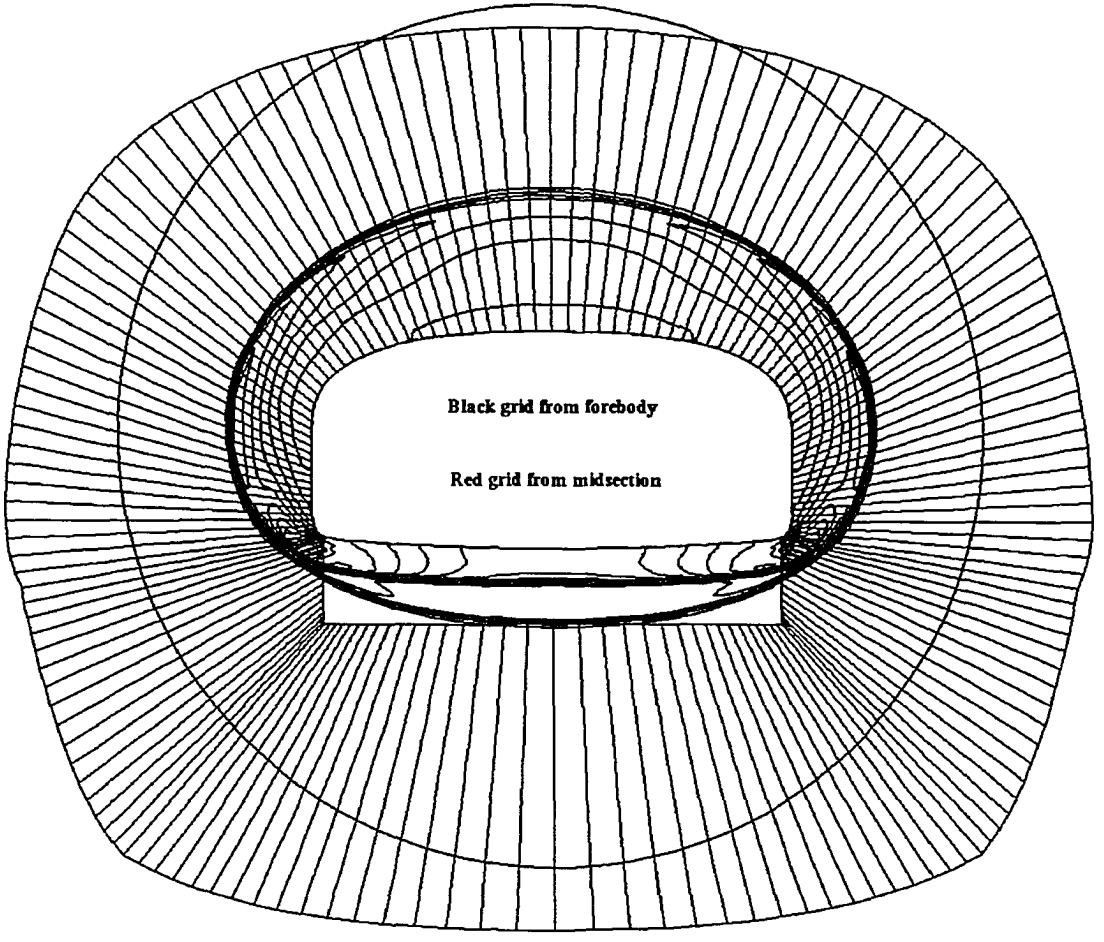


Figure 5.4: Pressure contours at the inlet plane of the scramjet depicting the shock-on-lip condition

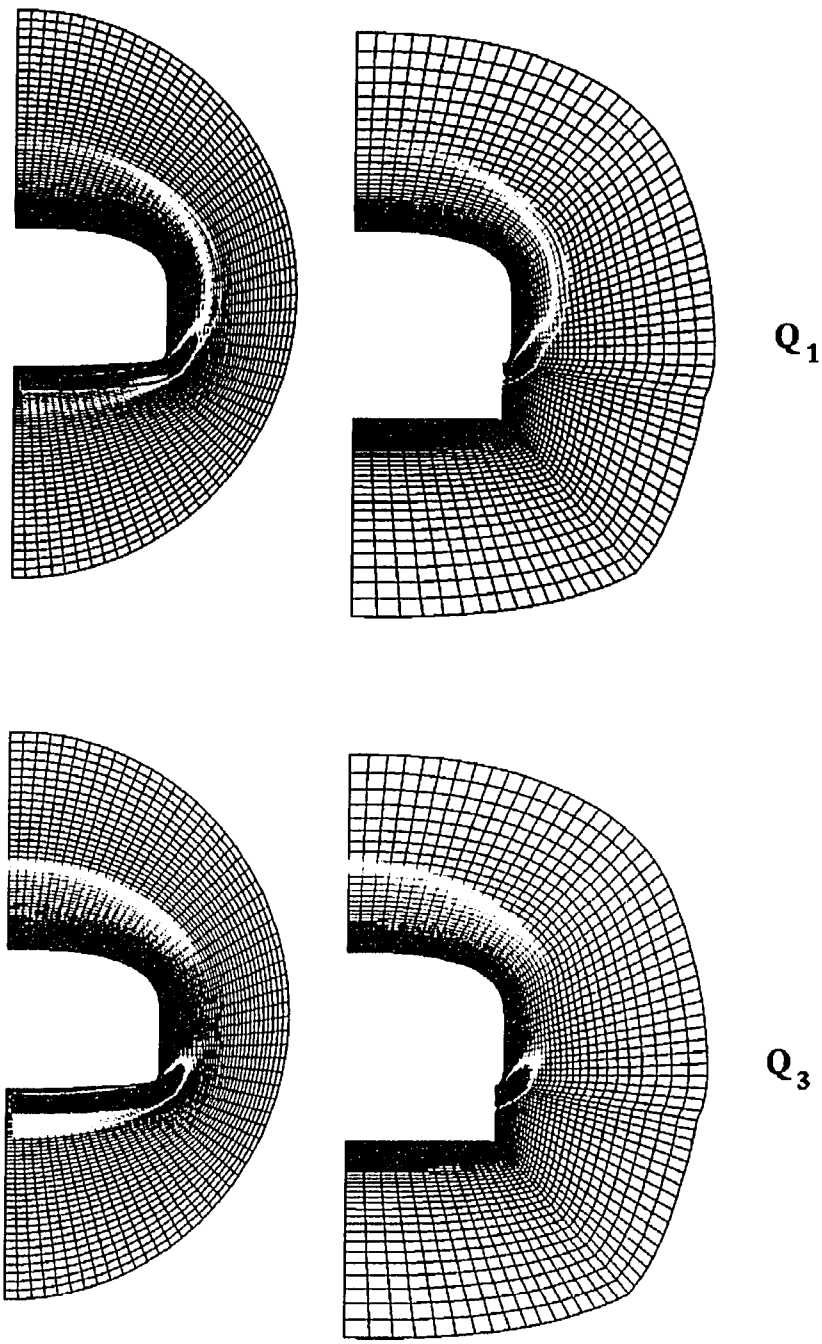


Figure 5.5: Interpolation of the Q-vectors ($Q_1$ and $Q_3$) from the forebody calculation onto the plane of the midsection grid at the inlet station of the scramjet

shock. These flow phenomena are illustrated in Fig. 5.6 using the Mach number contours in the symmetry plane of the scramjet engine and at the exit plane.

The pressure contours on the surface of the TTD geometry are shown in Fig. 5.7. The high pressures in the vicinity of the nose region and on the cowl lip (stagnation regions) are apparent. Figure 5.8 shows the Mach contours in the crossflow planes along the length of the body. Although the present cruise conditions result in a shock–on–lip condition, a portion of the shock emanating from the forebody compression corner enters the engine. Also, the vortices in the crossflow plane, shed from the sidewalls of the scramjet engine are clearly visible in the Mach contours on the underside of the aftbody in Fig. 5.8.

The average CPU times and step sizes of the flow calculations for the various sections of the TTD configuration are tabulated in Table 5.2. It should be pointed out that at the beginning of each calculation the step size was ramped up, typically in 100 steps, to the maximum step size indicated in Table 5.2. The total computation took 2 hours 9 minutes on a CRAY–YMP.

Table 5.2: Average CPU times and spatial step sizes for power-off calculation

| TTD section | x-loc. (m) | | Type of flow | | Maximum step size (m) | Avg. CPU time /step/grid point (s) |
|---|---|---|---|---|---|---|
| | Start | End | Ext. | Int. | | |
| Forebody | 0.012803 | 0.368300 | × | | $3.0\times10^{-4}$ | $2.7\times10^{-4}$ |
| Midsection | 0.368300 | 0.546100 | × | | $3.0\times10^{-4}$ | $2.7\times10^{-4}$ |
| Engine | 0.368300 | 0.546100 | | × | $7.0\times10^{-5}$ | $2.7\times10^{-4}$ |
| Aftbody | 0.546100 | 0.850000 | × | | $1.0\times10^{-4}$ | $2.7\times10^{-4}$ |

**Test case II**

This test case simulates a power-on case. A stoichiometric amount of $H_2$ fuel was injected across the crossflow plane at the throat (x = 0.46 m) of the scramjet. The fuel is added at a static temperature of 2000 K. For simplicity of analysis, the velocity vector of

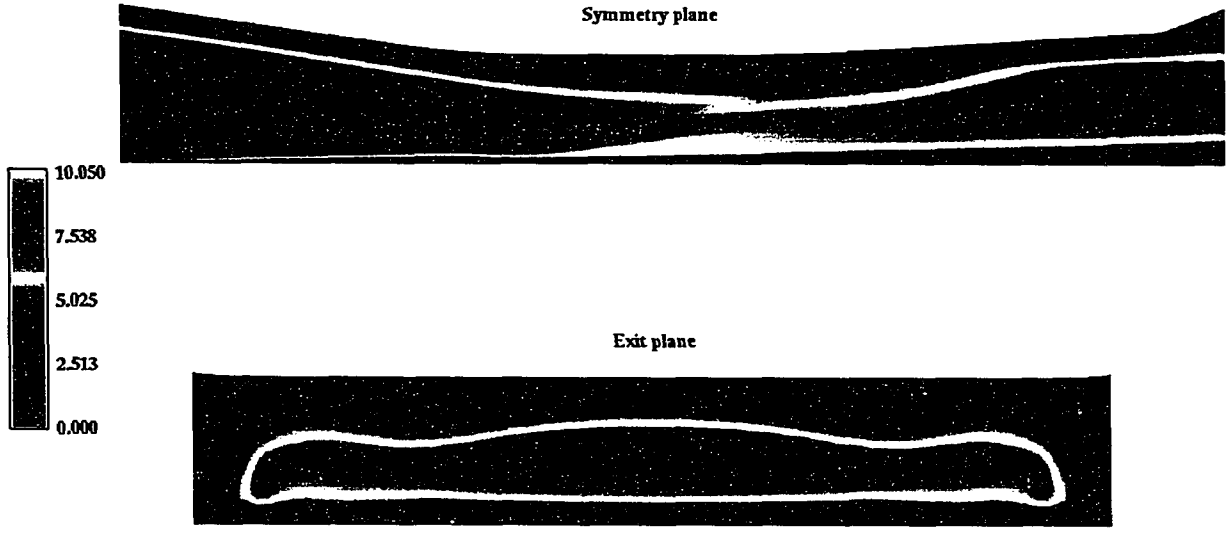


Figure 5.6: Mach contours in the symmetry plane and the exit plane of the scramjet for power-off calculation

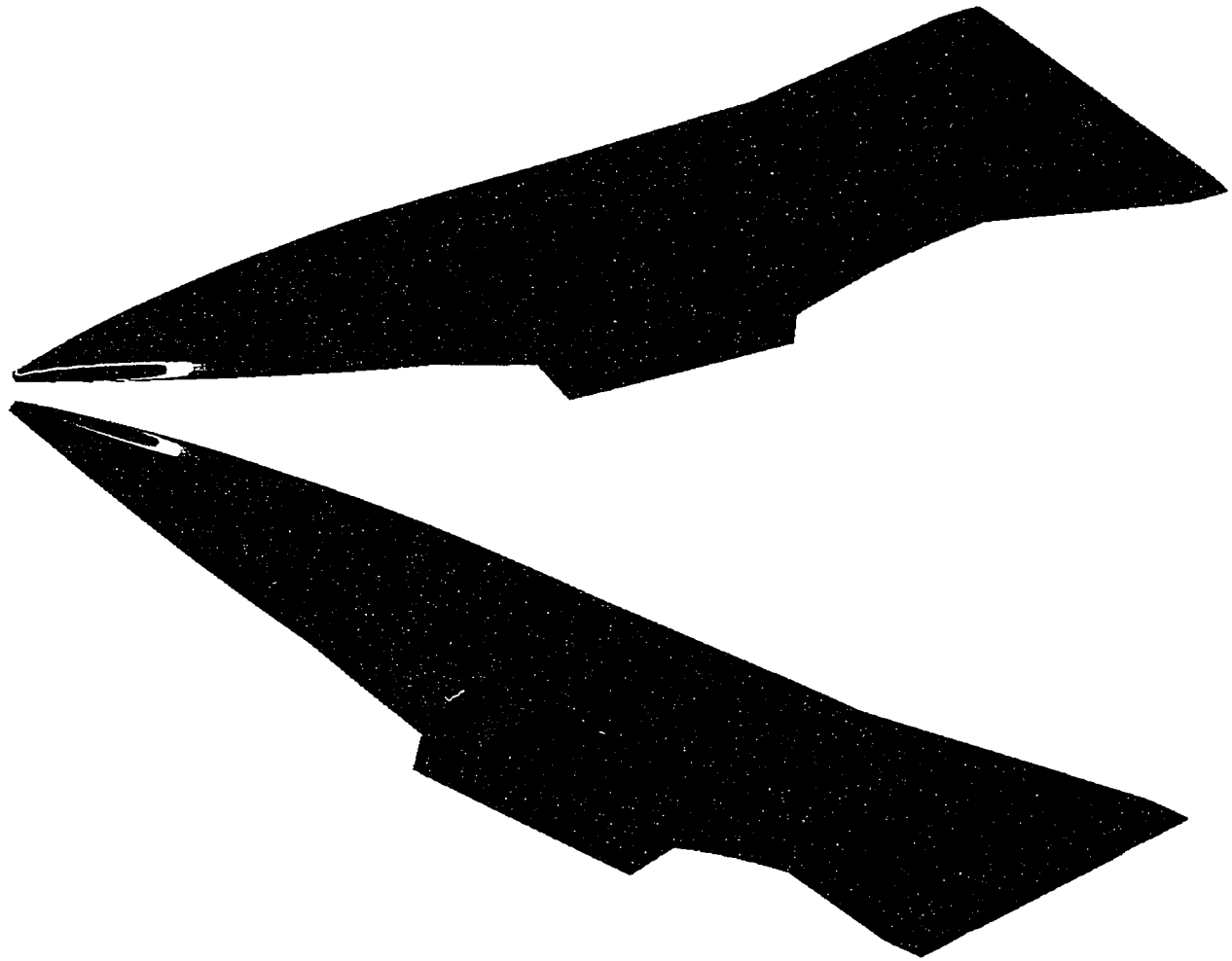

Figure 5.7: Surface pressure contours for power-off calculation

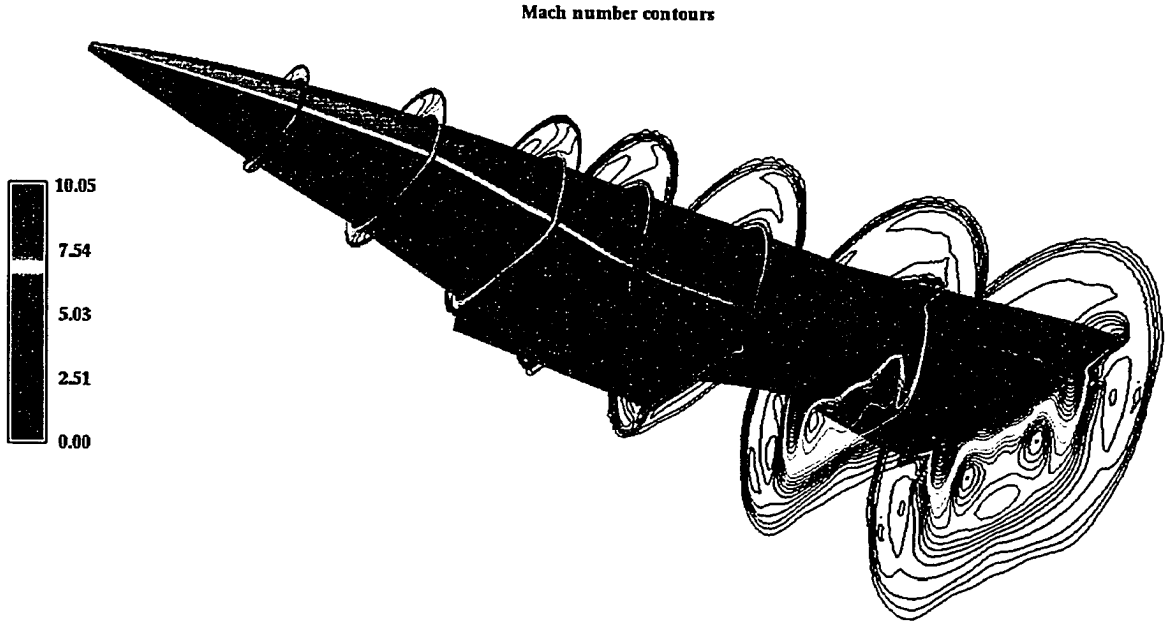


Figure 5.8: Mach contours in various crossflow planes along the length of the TTD configuration for power-off calculation

the added fuel is taken to be the same as the local air flow. The addition of fuel results in the addition of mass and enthalpy to the flowfield. These factors are taken into account by updating the density and energy at every grid point in the injection plane. Also to assist in the ignition process, a small amount of free radicals (H atoms) was added to the flowfield along with the fuel. This was found necessary because of the simplified geometry of the scramjet engine used in this study. These free radicals enhance the chain–branching reactions. The mass and enthalpy were adjusted to account for the addition of the free radicals.

As the flow conditions were chosen to be the same as that for the power-off calculation, the forebody and the external flow over the midsection remain the same as in Test case I. For the power-on simulation, average CPU timings and step sizes for the tip-to-tail calculation are tabulated in Table 5.3. As in Test case I, the step size is ramped up, typically in 100 steps, to the maximum step size indicated in Table 5.3.

Table 5.3: Average CPU times[a] and spatial step sizes for power-on calculation

| TTD section | x-loc. (m) | | Type of flow | | Maximum step size (m) | Avg. CPU time /step/grid point (s) |
|---|---|---|---|---|---|---|
| | Start | End | Ext. | Int. | | |
| Forebody | 0.012803 | 0.368300 | × | | $3.0\times10^{-4}$ | $2.7\times10^{-4}$ |
| Midsection | 0.368300 | 0.546100 | × | | $3.0\times10^{-4}$ | $2.7\times10^{-4}$ |
| Engine | 0.368300 | 0.546100 | | × | $7.0\times10^{-5}$ | $3.5\times10^{-4}$ |
| Aftbody | 0.546100 | 0.850000 | × | | $1.0\times10^{-4}$ | $2.0\times10^{-4}$ |

[a]The engine and aftbody calculations were performed on a CRAY C–90.

The water vapor mass fraction contours in the symmetry plane and the exit plane of the scramjet are shown in Fig. 5.9. The picture clearly shows that the combustion, indicated by the production of water vapor, is mainly occurring in the vicinity of the walls. The flowfield in the core region of the scramjet engine is unaffected. For this simplified

scramjet configuration, the freestream flight conditions are not severe enough to raise the temperature of the air to cause more rapid combustion. In a more realistic scramjet configuration, other mechanisms are provided to further compress the incoming air and augment the mixing of fuel and air.

In Fig. 5.10, the water vapor mass fraction contours are shown in two crossflow planes of the aftbody nozzle: one midway along the aftbody and one at the last station of the configuration. It can be observed that because of the expansion of the flow in the external nozzle, the extent of the water vapor reaches further out in the flowfield.

The Mach contours in the crossflow planes along the length of the body are shown in Fig. 5.11. It is interesting to compare the shock structure in the aftbody region for the power-off and power-on cases. This is shown in Fig. 5.12. Due to the high temperature and pressure of the combustion products, the exhaust from the scramjet is underexpanded and thus is expanding through the external nozzle region. This results in the shock (on the underside) being pushed further down in the power-on case. Also, it can be observed that the bottom portion of the shock is much stronger in the power-on case as compared to the power-off case.

The total tip–to–tail computation time for this case was 1 hour 30 minutes and it was computed partly on a CRAY–YMP and partly on a CRAY–C90. If the computations were performed entirely on a CRAY–YMP, the equivalent computation time would have been 2 hours 38 minutes.

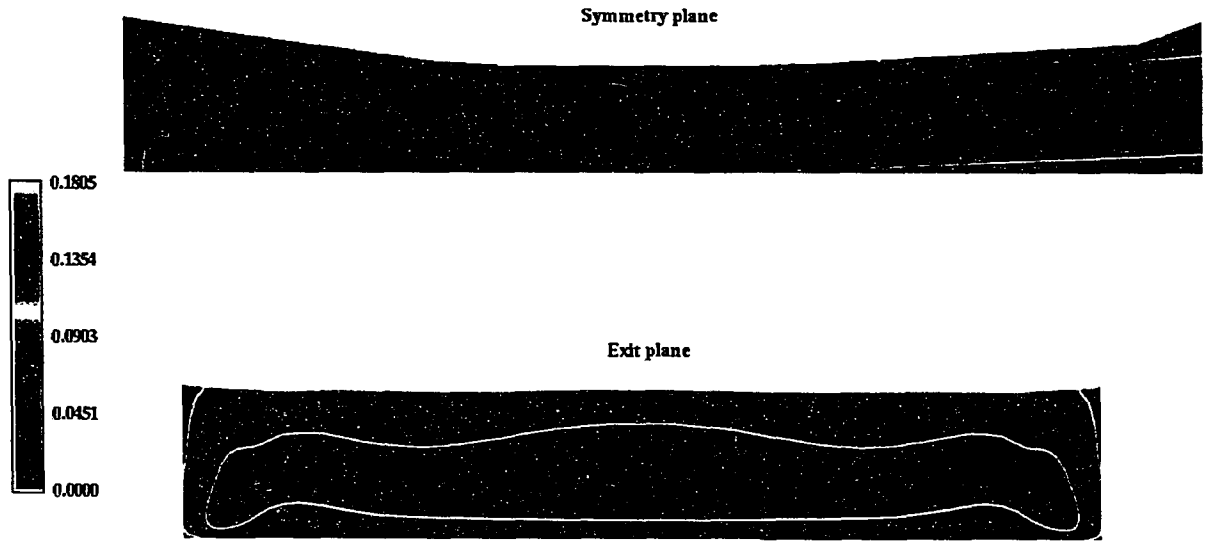


Figure 5.9: $H_2O$ mass fraction contours in the symmetry plane and the exit plane of the scramjet for power-on calculation

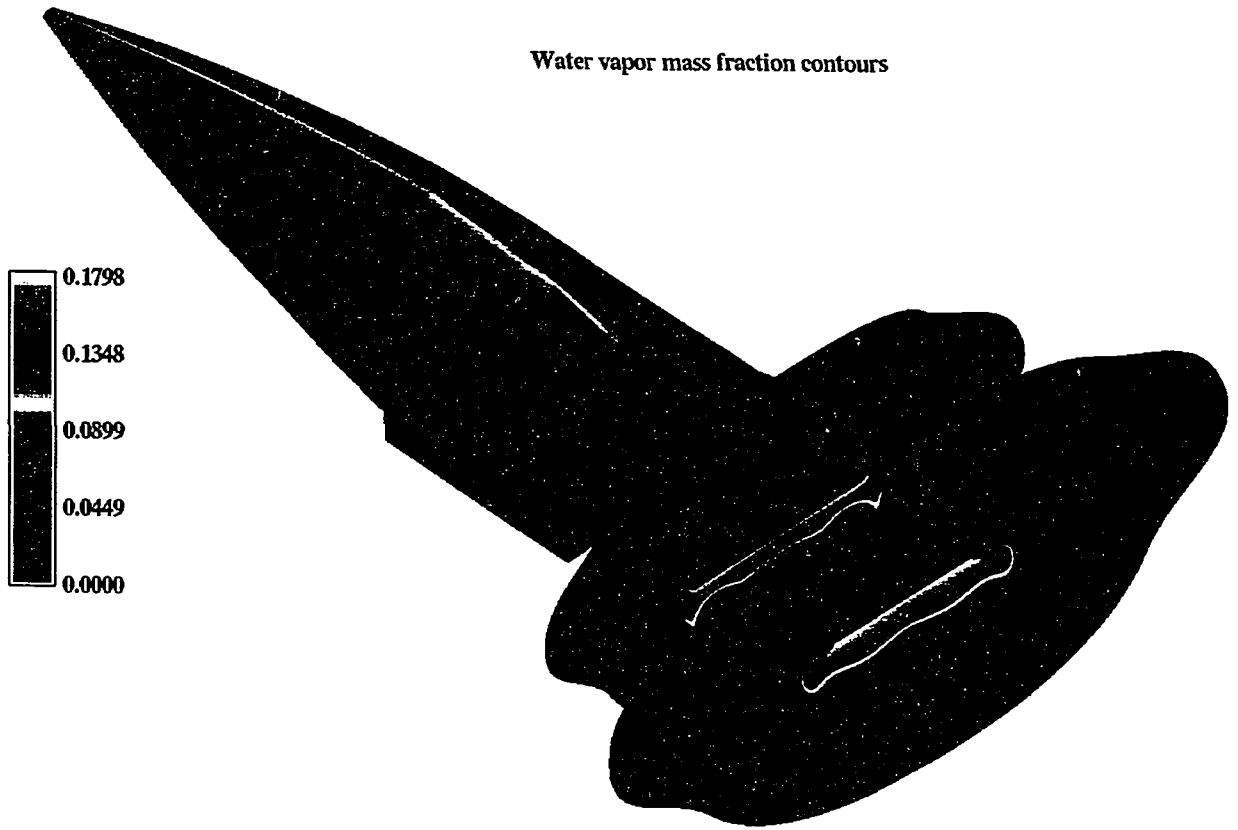


Figure 5.10: $H_2O$ mass fraction contours in the crossflow planes of the aftbody for power-on calculation

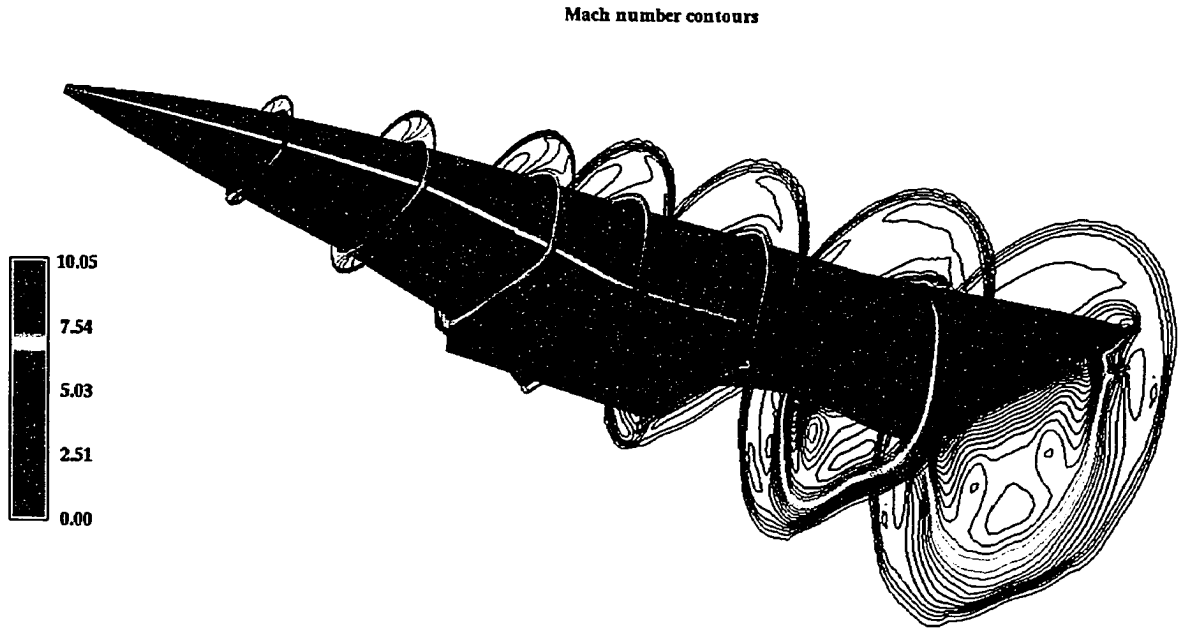


Figure 5.11: Mach contours in various crossflow planes along the length of the TTD configuration for power-on calculation

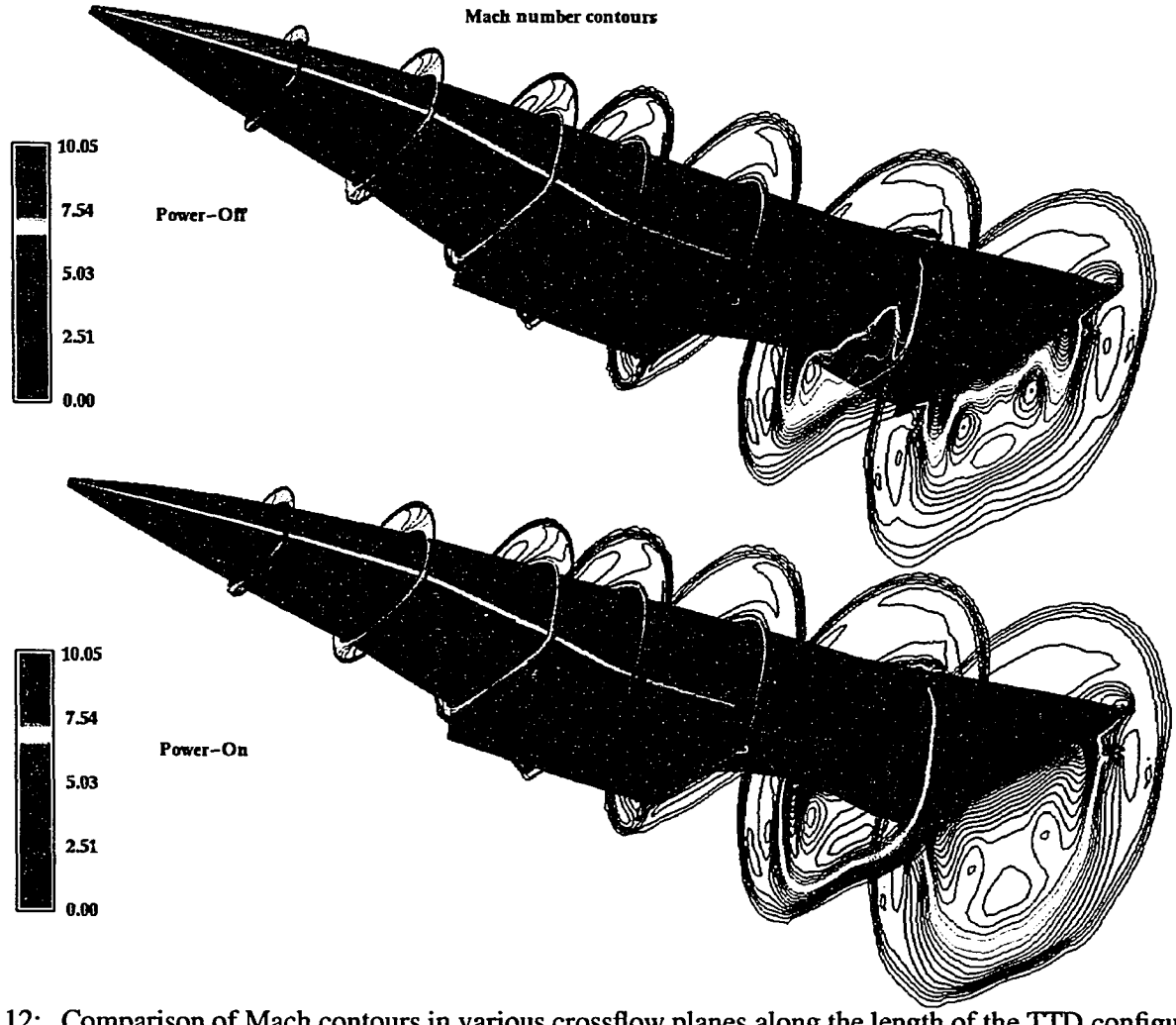


Figure 5.12: Comparison of Mach contours in various crossflow planes along the length of the TTD configuration for power-off and power-on calculations

# CHAPTER 6. CONCLUDING REMARKS

The three–dimensional UPS code has been extended in the present study to solve internal turbulent flows with hydrogen–air chemistry. The code now has the capability to compute both external and internal flows. Four gas options are available namely, perfect gas, equilibrium air, nonequilibrium air, and nonequilibrium hydrogen–air chemistry. The upwind scheme used in the UPS code makes it very robust and the dissipation associated with this scheme is sufficiently adaptive to various flow conditions. This eliminates the need for user–specified smoothing which is an integral part of all central differenced schemes.

In high–speed combustion flows, the turbulence enhanced mixing plays a critical role in the combustion process. Hence it is necessary to model the turbulence in the flowfield accurately. Two types of turbulence models have been incorporated into the code. A modified Baldwin–Lomax algebraic turbulence model has been included to handle configurations with multiple walls. In addition, the two–equation ($k - \epsilon$) turbulence model of Jones–Launder has been incorporated. The turbulence transport equations of Jones–Launder are solved in a loosely–coupled manner. The user has the option of choosing the low Reynolds number form of the equations for configurations with no–slip boundary conditions or the high Reynolds number form of the equations for free–shear layer type of applications. Although there is an increase in computation time and effort, the two–equation turbulence model has a distinct advantage over algebraic turbulence models in the ability

to simulate corner flows and free–shear layer flows which are typically encountered in scramjet flowfields. For such flows, algebraic turbulence models require user specification of length scales. These length scales are problem dependent and require a knowledge of the flowfield. Two–equation turbulence models, on the other hand, solve for the length scales implicitly.

Various test cases have been calculated to validate the hydrogen–air capability and the turbulence models. For the two–equation model, both the low and high Reynolds number form of the equations have been tested, both with perfect gas as well as finite–rate chemistry options. The computed results are in good agreement with the available experimental data, and the analytical and numerical solutions.

The flow about hypersonic space planes is very complex. The modifications and enhancements made to the UPS code have been applied to several component test cases. In the present study, the various capabilities of the UPS code have been combined to compute the complete tip-to-tail solution of the integrated aerodynamic and propulsive flowfields of the Test Technology Demonstrator (TTD), a generic hypersonic vehicle geometry. Two demonstration test cases, one with power-off and one with power-on, have been computed. A substantial savings in the computing time and storage have been achieved by using the parabolized Navier–Stokes equations instead of the unsteady Navier–Stokes equations. The savings achieved can be resourcefully channelled towards increasing the complexity of the numerical or geometric models and/or simulating a battery of flight conditions.

For treating realistic scramjet configurations, which have a setback cowl plate and multiple modules with planar or swept sidewall compression, a zonal capability with multiple block grids in the crossflow plane is needed. This would make the grid generation procedure much simpler and would also provide the capability of local enrichment of

the modular grid where needed. The actual fuel injection process is more complicated than assumed in this demonstration. The injection of the fuel is typically performed in multiple stages with injectors placed at an angle or transverse to the flow. The bow shock produced upstream of such an injection provides increased pressure and temperature, and the recirculating region downstream of the injection results in enhanced penetration and mixing of the fuel and air. Both these factors aid in the combustion process and increase the efficiency of the scramjet engine. As the scenario described above results in subsonic inviscid regions and streamwise separated regions, it would become necessary to use an unsteady Navier–Stokes (NS) solver for the analysis. The optimum choice is to couple both the NS and PNS solvers in such a way that the PNS solver can be used in all the regions where the inviscid region is supersonic and there is no streamwise separation. This will minimize the prohibitive computational costs associated with the NS solvers. This study has demonstrated that the UPS code is a very valuable tool in the design and analysis of hypersonic space planes and scramjet engines.

## REFERENCES

[1] Edwards, C. L. W., Small, W. J., Weidner, J. P., and Johnston, P. J. "Studies of Scramjet/Airframe Integration Techniques for Hypersonic Aircraft." AIAA–75–58. Aerospace Sciences Meeting, Jan. 20–22, 1975, Pasadena, California.

[2] Henry, J. R., and Anderson, G. Y. "Design Considerations for the Airframe–Integrated Scramjet." NASA TMX–2895. Dec. 1973.

[3] Murthy, S. N. B., and Curran, E. T. "*High–Speed Flight Propulsion Systems.*" Washington D. C.: American Institute of Aeronautics and Astronautics, 1991.

[4] Gnoffo, P. A., and McCandless, R. S. "Three Dimensional AOTV Flowfields in Chemical Nonequilibrium." AIAA–86–0230. Aerospace Sciences Meeting, Jan. 6–9, 1986, Reno, Nevada.

[5] Candler, G. V., and MacCormack, R. W. "The Computation of Hypersonic Ionized Flows in Chemical and Thermal Nonequilibrium." AIAA–88–0511. Aerospace Sciences Meeting, Jan. 11–14, 1988, Reno, Nevada.

[6] Palaniswamy, S., Chakravarthy, S. R., and Ota, D. K. "Finite–Rate Chemistry for USA–Series Code: Formulation and Applications." AIAA– 89–0200. Aerospace Sciences Meeting, Jan. 9–12, 1989, Reno, Nevada.

[7] Shuen, J. S., and Liou, M. S. "Flux-Splitting Algorithms for Two–Dimensional Viscous Flows with Finite–Rate Chemistry." AIAA–89–0388. Aerospace Sciences Meeting, Jan. 9–12, 1989, Reno, Nevada.

[8] Yu, S. T., Tsai, Y. L. P., and Shuen, J. S. "Three-Dimensional Calculation of Supersonic Reacting Flows Using an LU Scheme." AIAA–89–0391. Aerospace Sciences Meeting, Jan. 9–12, 1989, Reno, Nevada.

[9] Palmer, G. "An Efficient, Explicit Finite-Rate Algorithm to Compute Flows in Chemical Nonequilibrium." AIAA–89–0522. Aerospace Sciences Meeting, Jan. 9–12, 1989, Reno, Nevada.

[10] Hoffman, J. J. "Development of an Algorithm for the Three–Dimensional Fully–Coupled Navier–Stokes Equations with Finite–Rate Chemistry." AIAA–89–0670. Aerospace Sciences Meeting, Jan. 9–12, 1989, Reno, Nevada.

[11] Molvik, G. A., and Merkle, C. L. "A Set of Strongly–Coupled Upwind Algorithms for Computing Flows in Chemical Nonequilibrium." AIAA–89–0199. Aerospace Sciences Meeting, Jan. 9–12, 1989, Reno, Nevada.

[12] Imlay, S. T., Roberts, D. W., Soetrisno, M., and Eberhardt, S. "Nonequilibrium Thermo–Chemical Calculations using a Diagonal Implicit Scheme." AIAA–91–0468. Aerospace Sciences Meeting, Jan. 7–10, 1991, Reno, Nevada.

[13] Withington, J. P., Shuen, J. S., and Yang, V. "A Time Accurate Implicit Method for Chemically Reacting Flows at All Mach Numbers." AIAA–91–0581. Aerospace Sciences Meeting, Jan. 7–10, 1991, Reno, Nevada.

[14] Walters, R. W., Cinnella, P., Slack, D. C., and Halt, D. "Characteristic Based Algorithms for Flows in Thermochemical Non-equilibrium." *AIAA Journal*, 30, No. 5(1992): 1304–1313.

[15] Bhutta, B. A., Lewis, C. H., and Kautz II, F. A. "A Fast Fully–Iterative Parabolized Navier–Sokes Scheme for Chemically–Reacting Reentry Flows." AIAA–85–0926. June 1985.

[16] Bhutta, B. A., and Lewis, C. H. "Three Dimensional Hypersonic Nonequilibrium Flows at Large Angles of Attack." *Journal of Spacecraft and Rockets*, 26, No. 3(1989): 158–166.

[17] Prabhu, D. K., Tannehill, J. C., and Marvin, J. G. "A New PNS Code for Chemical Nonequilibrium Flows." *AIAA Journal*, 26, No. 7(1988): 808–815.

[18] Prabhu, D. K., Tannehill, J. C., and Marvin, J. G. "A New PNS Code for Three–Dimensional Chemically Reacting Flows." *Journal of Thermophysics and Heat Transfer*, 4, No. 3(1990): 257–258.

[19] Sinha, N., Dash, S. M., and Krawczyk, W. J. "Inclusion of Chemical Kinetics into Beam–Warming Based PNS Model for Hypersonic Propulsion Applications." AIAA–87–1898. Joint Propulsion Conference, June 29–July 2, 1987, San Diego, California.

[20] Korte, J. J., and McRae, D. S. "Explicit Upwind Algorithm for the Parabolized Navier–Stokes Equations." AIAA–88–0716. Aerospace Sciences Meeting, Jan. 11–14, 1988, Reno, Nevada.

[21] Chitsomboon, T., and Northam, G. B. "A 3D-PNS Computer Code for the Calculation of Supersonic Combusting Flows." AIAA–88–0438. Aerospace Sciences Meeting, Jan. 11–14, 1988, Reno, Nevada.

[22] Tannehill, J. C., Ievalts, J. O., and Lawrence, S. L. "An Upwind Parabolized Navier–Stokes Code for Real Gas Flows." AIAA–88–0713. Aerospace Sciences Meeting, Jan. 11–14, 1988, Reno, Nevada.

[23] Tannehill, J. C., Ievalts, J. O., Buelow, P. E., Prabhu, D. K., and Lawrence, S. L. "Upwind Parabolized Navier–Stokes Code for Chemically Reacting Flows." *Journal of Thermophysics and Heat Transfer*, 4, No. 2(1990): 149–156.

[24] Gielda, T., and Agarwal. R. "Efficient Finite-Volume Parabolized Navier-Stokes Solutions for Three-Dimensional, Hypersonic, Chemically Reacting Flowfields." AIAA–89–0103. Aerospace Sciences Meeting, Jan. 9–12, 1989, Reno, Nevada.

[25] Kamath, H. "Parabolized Navier-Stokes Algorithm for Chemically Reacting Flows." AIAA–89–0386. Aerospace Sciences Meeting, Jan. 9–12, 1989, Reno, Nevada.

[26] Liou, M. F. "Three Dimensional PNS Solutions of Hypersonic Internal Flows with Equilibrium Chemistry." AIAA–89–0002. Aerospace Sciences Meeting, Jan. 9–12, 1989, Reno, Nevada.

[27] Sinha, N., Dash, S. M., and Lee, R. A. "3–D PNS Analysis of Scramjet Combustion/Nozzle And Exhaust Plume Flowfields." AIAA–90–0094. Aerospace Sciences Meeting, Jan. 1990, Reno, Nevada.

[28] Tannehill, J. C., Buelow, P. E., Ievalts, J. O., and Lawrence, S. L. "Three–Dimensional Upwind Parabolized Navier–Stokes Code for Real Gas Flows." *Journal of Spacecraft and Rockets*, 27, No. 2(1990): 150–159.

[29] Gerbsch, R. A., and Agarwal, R. K. "Solution of the Parabolized Navier–Stokes Equations for Three-Dimensional Real–Gas Flows using Osher's Upwind Scheme." AIAA–91–0248. Aerospace Sciences Meeting, Jan. 7–10, 1991, Reno, Nevada.

[30] Buelow, P. E., Tannehill, J. C., Ievalts, J. O., and Lawrence, S. L. " A Three–Dimensional, Upwind, Parabolized Navier–Stokes Code for Chemically Reacting Flows." *Journal of Thermophysics and Heat Transfer*, 5, No. 3(1991): 274–283.

[31] Lawrence, S. L., Tannehill, J. C., and Chaussee, D. S. "Upwind Algorithm for the Parabolized Navier–Stokes Equations." *AIAA Journal*, 27, No. 9(1989) 1175–1183.

[32] Lawrence, S. L., Chaussee, D. S., and Tannehill, J. C. "Application of an Upwind Algorithm to the Three–Dimensional Parabolized Navier–Stokes Equations." *AIAA Journal*, 28, No. 6(1990): 971–972.

[33] Roe, P. L. "Approximate Riemann Solvers, Parameter Vectors, and Difference Schemes." *Journal of Computational Physics*, 43(1983): 357–372.

[34] Buelow, P. E., Ievalts, J. O., and Tannehill, J. C. "Comparison of Three–Dimensional Nonequilibrium PNS Codes." AIAA–90–1572. Fluid Dynamics, Plasma Dynamics & Lasers Conference, June 18–20, 1990, Seattle, Washington.

[35] Lawrence, S. L. "Numerical Performance Estimates For a Generic Hypersonic Forebody." AIAA–91–1695. Fluid Dynamics, Plasma Dynamics & Lasers Conference, June 24–26, 1991, Honolulu, Hawaii.

[36] Lockman, W. K., Lawrence, S. L., and Cleary, J. W. "Flow Over an All–Body Hypersonic Aircraft: Experiment and Computation." *Journal of Spacecraft and Rockets*, 29, No. 1(1992): 7–15.

[37] Wadawadigi, G., Tannehill, J. C., Buelow, P. E., and Lawrence, S. L. "A Three–Dimensional Upwind PNS Code for Chemically Reacting Scramjet Flowfields." AIAA–92–2898. Thermophysics Conference, July 6–8, 1992, Nashville, Tennessee. (Also *Journal of Thermophysics and Heat Transfer*, 7, No. 4(1993): 661–667)

[38] NASP Rate Constant Committee. "Hypersonic Combustion Kinetics: Status Report Of The Rate Constant Committee." NASP High Speed Propulsion Technology Team. NASP TM–1107. 1990.

[39] Baldwin, B. S., and Lomax, H. "Thin Layer Approximation and Algebraic Model for Separated Turbulent Flows." AIAA Paper 78–257. Aerospace Sciences Meeting, Jan. 16–18, 1978, Huntsville, Alabama.

[40] Hung, C. –M., and Buning, P. G. "Simulation of Blunt–Fin–Induced Shock–Wave and Turbulent Boundary–Layer Interaction." *Journal of Fluid Mechanics*, 154(1985): 163–185.

[41] Jones, W. P. and Launder, B. E. "The Prediction of Laminarization with a Two–Equation Model of Turbulence." *International Journal of Heat and Mass Transfer*, 15(1972): 303–314.

[42] Zeman, O. "Dilatation dissipation: The Concept and Application in Modeling Compressible Mixing Layer." *Physics of Fluids A*, 2, No. 2(Feb. 1990): 178–188.

[43] Sarkar, S., and Balakrishnan, L. "Application of a Reynolds Stress Turbulence Model to the Compressible Shear Layer." ICASE Report No. 90–18. Feb. 1990.

[44] Burrows, M. C., and Kurkov, A. P. "Analytical and Experimental Study of Supersonic Combustion of Hydrogen in a Vitiated Airstream." NASA TM X–2828. Sept. 1973.

[45] Wadawadigi, G., Tannehill, J. C., Edwards, T. A., Lawrence, S. L., and Molvik, G. A. "Application of a Two–Equation Turbulence Model to Supersonic Combustion Flowfields." AIAA–94–0705. Aerospace Sciences Meeting, Jan. 10–13, 1994, Reno, Nevada.

[46] Viegas, J. R., and Rubesin, M. W. "A Comparative Study of Several Compressibility Corrections to Turbulence Models Applied to High–Speed Shear Layers." AIAA–91–1783. Fluid Dynamics, Plasma Dynamics & Lasers Conference, June 24–26, 1991, Honolulu, Hawaii.

[47] Van Driest, E. R. "The Problem of Aerodynamic Heating." *Aeronautical Engineering Review*, 15, No. 10(1956): 26–41.

[48] Private communications with Dr. Johnny R. Narayan, Research Scientist, MCAT Institute, NASA Ames Research Center.

[49] Wadawadigi, G., Tannehill, J. C., Lawrence, S. L., and Edwards, T. A. "Three–Dimensional Computation of the Integrated Aerodynamic and Propulsive Flowfields of a Generic Hypersonic Space Plane." AIAA–94–0633. Aerospace Sciences Meeting, Jan. 10–13, 1994, Reno, Nevada.

[50] Vigneron, Y. C., Rakich, J. V., and Tannehill, J. C. "Calculation of Supersonic Flow over Delta Wings with Sharp Subsonic Leading Edges." AIAA–78–1137. Fluid and Plasma Dynamics Conference, July 10–12, 1978, Seattle, Washington.

[51] McBride, B. J., Heimel, S., Ehlers, J. G., and Gordon, S. "Thermodynamic Properties to 6000°K for 210 Substances Involving the First 18 Elements." NASA SP–3001. 1963.

[52] Svehla, R. A. "Estimated Viscosities And Thermal Conductivities Of Gases At High Temperatures." NASA TR R–132. 1962.

[53] Wilke, C. R. "A Viscosity Equation for Gas Mixtures." *Journal of Chemical Physics*, 18(April 1950): pp. 517.

[54] Strehlow, R. A. "*Combustion Fundamentals.*" New York: McGraw-Hill Book Company, 1984.

[55] Kuo, K. K. "*Principles of Combustion.*" New York: John Wiley & Sons, 1986.

[56] Blottner, F. G., Johnson, M., and Ellis, M. "Chemically Reacting Viscous Flow Program for Multi-Component Gas Mixtures." Report No. SC–RR–70–754. Sandia Laboratories, Albuquerque, New Mexico, Dec. 1971.

[57] Gardiner, W. C. Jr. "*Combustion Chemistry.*" New York: Springer–Verlag, 1984.

[58] Hung, C. –M., and MacCormack, R. W. " Numerical Solution of Three–Dimensional Shock Wave and Boundary Layer Interaction." *AIAA Journal,* 16(1979): 1090–1096.

[59] Ladd, J. A., and Kral, L. D. "Development and Application of a Zonal $k-\epsilon$ Turbulence Model for Complex 3–D Flowfields." AIAA 92–3176. Joint Propulsion Conference, July 6–8, 1992, Nashville, Tennessee.

[60] Lawrence, S. L. "Application of Space–Marching Methods to Hypersonic Forebody Flow Fields." AIAA–92–5030. International Aerospace Conference, Dec. 1–4, 1992, Orlando, Florida.